

UC Santa Cruz

UC Santa Cruz Electronic Theses and Dissertations

Title

Precision Measurement of the Strong Coupling Constant of the Minimal Universal Extra Dimensions Model Using Like-Sign Leptons at the Large Hadron Collider

Permalink

<https://escholarship.org/uc/item/8s99t14d>

Author

Fava, Laura

Publication Date

2015

Peer reviewed|Thesis/dissertation

UNIVERSITY OF CALIFORNIA
SANTA CRUZ

**PRECISION MEASUREMENT OF THE STRONG COUPLING
CONSTANT OF THE MINIMAL UNIVERSAL EXTRA
DIMENSIONS MODEL USING LIKE-SIGN LEPTONS AT THE
LARGE HADRON COLLIDER**

A dissertation submitted in partial satisfaction of the
requirements for the degree of

DOCTOR OF PHILOSOPHY

in

PHYSICS

by

Laura Fava

June 2015

The Dissertation of Laura Fava
is approved:

Professor Howard E. Haber, Chair

Professor Jason Nielsen

Professor Stefano Profumo

Tyrus Miller
Vice Provost and Dean of Graduate Studies

Copyright © by

Laura Fava

2015

Table of Contents

List of Figures	v
List of Tables	vi
Abstract	vii
Dedication	viii
Acknowledgments	ix
1 Introduction	1
1.1 The Standard Model	2
1.2 Beyond the Standard Model	7
2 Review of Universal Extra Dimensions	16
2.1 General Features of UED	17
2.2 Minimal UED	21
3 Precision Measurement at the LHC	28
3.1 Analysis Scheme	28
3.2 Precision measurement of UED strong coupling	30
3.2.1 Kaluza-Klein quark and gluon production at the LHC	31
3.2.2 Major Backgrounds and Signal Selection	34
3.2.3 Sources of mUED signal uncertainty	39
3.2.4 Bounds on the g_{ued} measurement	41
3.3 Results of precision measurement of strong coupling	43
4 Conclusion	55
A Select Feynman Rules for mUED	58

B Statistical Methods	61
B.1 Method of Maximum Likelihood	64
B.2 Estimating cut efficiencies and their uncertainties using Bayesian statistics	71
Bibliography	75

List of Figures

2.1	Mass spectra for mUED	26
2.2	The $n = 1$ Kaluza-Klein decay chain for mUED	27
3.1	Feynman diagrams of $qq \rightarrow Q_1 g_1$	33
3.2	Feynman diagrams of $qq \rightarrow Q_1 Q_1$	33
3.3	mUED signal cross sections as a function of R^{-1}	36
3.4	Distribution of lepton p_T for mUED scenario: $R^{-1} = 800$ GeV, $\Lambda R = 20$	38
3.5	Bounds on g_{ued} : g_{ued}/g_{sm} vs. κ for $R^{-1} = 800$ GeV, $\Lambda R = 20$	44
3.6	Bounds on g_{ued} : g_{ued}/g_{sm} vs. κ for $R^{-1} = 900$ GeV, $\Lambda R = 20$	45
3.7	Bounds on g_{ued} : g_{ued}/g_{sm} vs. κ for $R^{-1} = 1000$ GeV, $\Lambda R = 20$	46
3.8	Bounds on g_{ued} : g_{ued}/g_{sm} vs. κ for $R^{-1} = 1100$ GeV, $\Lambda R = 20$	47
3.9	Bounds on g_{ued} : g_{ued}/g_{sm} vs. κ for $R^{-1} = 1200$ GeV, $\Lambda R = 20$	48
3.10	Bounds on g_{ued} : g_{ued}/g_{sm} vs. κ for $R^{-1} = 1300$ GeV, $\Lambda R = 20$	49
3.11	Bounds on g_{ued} : g_{ued}/g_{sm} vs. κ for $R^{-1} = 800$ GeV, $\Lambda R = 5$	50
B.1	Profile Likelihood Ratio and Posterior for S	70

List of Tables

3.1	Relevant branching ratios for mUED scenario: $R^{-1} = 800$ GeV and $\Lambda R = 20$	31
3.2	Cutflow for mUED scenario: $R^{-1} = 800$ GeV and $\Lambda R = 20$	37
3.3	Current assessment of mUED signal uncertainty	40
3.4	Bounds on g_{ued}/g_{sm} (Part 1)	51
3.5	Bounds on g_{ued}/g_{sm} (Part 2)	52
A.1	Feynman rules for colored KK particles.	59
A.2	Feynman rules for weakly and electromagnetically interacting KK particles.	60
B.1	Cutflow efficiencies	74

Abstract

Precision Measurement of the Strong Coupling Constant of the Minimal Universal Extra Dimensions Model Using Like-Sign Leptons at the Large Hadron Collider

by

Laura Fava

If new heavy particles are discovered at the Large Hadron Collider (LHC), we will need a way to distinguish among various theoretical interpretations for the new physics beyond the Standard Model (BSM). Models of BSM physics often predict specific relations that must be satisfied by the couplings of the new particles. For example, the coupling of the quark, Kaluza-Klein quark and Kaluza-Klein gluon of the minimal Universal Extra Dimensions (mUED) model must equal the strong coupling constant of QCD up to small symmetry-breaking corrections that are radiatively generated. Using computer simulations, I investigate the possible precision with which one can measure this coupling at the LHC by examining like-sign dilepton events that include additional hadronic jets and missing transverse energy. To set bounds on the precision of a measurement of the mUED strong coupling constant, I vary this constant away from its predicted value and investigate the resulting change to the number of events expected at the LHC. I show that a measurement of the mUED strong coupling constant can be constrained to $\sim 5 - 25\%$ provided the systematic uncertainty of the mUED signal can be reduced.

For Daniel and Lucas

Acknowledgments

I would like to thank my advisor, Howie Haber, who directed and supervised the research in this dissertation and whose insights and expertise were critical to its development. His passion and dedication to particle physics and teaching are inspiring, and I hope to feel the same about my work as I head into the future.

I would also like to thank Jason Nielsen for stepping in to the role of my advisor during my first year and for the many useful conversations about particle physics and statistics (and, of course, ROOT!) throughout my time at UCSC.

And thank you to Stefano Profumo who challenged me to understand theory on a deeper level.

Sebastian Grab started me on the long road of programming and event generators. As a result of his patient teaching, I was able to undertake this project.

I have been fortunate to spend my time at UCSC with an outstanding group of students. I am especially grateful for Rachel Rampy's years of support as a colleague and friend. My officemates over the years, Tim Linden, Max Wainwright, Chris Moody, Lauren Porter, Jonathan Cornell, Laurel Stephenson-Haskins, Adam Coogan, and Eric Carlson, have all contributed to my understanding of particle physics and always created a friendly environment. Many conversations with Jonathan were especially helpful. Finally, I want to thank Eddie Santos for his camaraderie and humor throughout our tenure together.

I would like to thank my parents for raising me to believe that I could ac-

compish whatever I put my mind to and my sister, Jen, for being a role model who demonstrated problem solving and intellectual capability right from the start.

The support and affection I receive from my friends has carried me through the many challenges of the PhD. Thank you to the DLG, and to Rachel Foster, Ramie Alkire, Sylvia Tewes, Carla Rebelo, Colleen Kron, and Nicole Moody for all your love and encouragement.

Finally, thank you to my husband Daniel. Thank you for your love and partnership and for (insisting on) teaching me python. I truly could not have done this without you.

Chapter 1

Introduction

On July 4, 2012, the ATLAS and CMS collaborations jointly announced the observation of a Higgs boson [1, 2], the last piece needed to make the Standard Model (SM) of particle physics a complete, self-contained theory. The SM is an elegant, robust, and well-tested theory of matter and three of its four fundamental interactions — strong, weak, and electromagnetic — all except gravity. But despite the phenomenal predictive track record of the SM, a number of questions about the physical nature of the universe go unresolved. The hierarchy problem, the mystery of the vast energy difference between the electroweak scale (~ 100 GeV) and the Planck scale, the fundamental scale of gravitational interactions ($\sim 10^{19}$ GeV), cannot be solved without additional dynamics originating outside the SM. Baryonic matter, matter composed from the quarks and leptons of the SM, accounts for only 15.5% of the matter in the universe, the remainder of which is called dark matter and whose nature is currently unknown [3]. The SM predicts massless neutrinos, but observed neutrino oscillations imply that neutrinos have

mass. Furthermore, the SM provides no explanation for the asymmetry of baryons in the universe. Attempts to address these outstanding problems require us to look to theories beyond the Standard Model (BSM) with new physics that enters at the TeV scale, now accessible at the Large Hadron Collider (LHC) [4, 5, 6, 7, 8, 9, 10, 11, 12, 13]. Many BSM models include a stable dark matter candidate, a long-sought particle which makes up part or all of the missing matter content of the universe, and which can provide a promising signature for searches at the LHC. Prevalent classes of BSM theories include supersymmetry, strongly interacting dynamics for electroweak symmetry breaking, and theories of extra dimensions. If evidence for BSM physics is discovered at the LHC, the challenge will be to determine the correct theoretical interpretation. Different theories can predict similar signatures [14], so establishing techniques that favor or disfavor competing paradigms is crucial.

1.1 The Standard Model

The Standard Model of particle physics describes the fundamental particles and their electromagnetic (EM), weak, and strong interactions. The leptons and quarks are the fundamental fermions of the theory. There are three mass generations of the quarks and leptons, as well as an antiparticle corresponding to each particle. Each generation of quarks is composed of an up-type quark and a down-type quark. The up u , charm c , and top t quarks are up-type quarks, while down d , strange s , and bottom b are down-type quarks. The quarks can interact with all the bosons. Each generation

of leptons contains an electrically charged lepton, the electron e , muon μ , or the tau lepton τ , and an electrically neutral lepton called a neutrino, whose flavors correspond to the charged leptons, ν_e , ν_μ , and ν_τ . Both the charged and neutral leptons can interact with the weak force, but they carry no color charge and therefore do not interact via the strong force. Members of the lightest generation are stable and make up all the baryonic and atomic matter in the universe —the stars, the planets, the earth and all its inhabitants.

Interactions between the fundamental particles are mediated by gauge bosons. The massless photon mediates the familiar electromagnetic force, responsible for all of chemistry and most of the everyday forces we observe (other than gravity). There are eight massless gluons that mediate the strong force, the force that binds quarks together into mesons and baryons and keeps atomic nuclei together. The weak interactions, responsible for most radioactive decays, are mediated by the massive charged W^+ and W^- and neutral Z vector bosons.

The SM also contains the scalar Higgs boson. The Higgs is an excitation of the field whose non-zero vacuum expectation value is responsible for electroweak symmetry breaking (EWSB), as well as generating mass terms for the W^\pm and Z gauge bosons. The Higgs field also generates mass terms for the fermions (except the neutrinos) through Yukawa interactions. The mass of the Higgs boson itself comes from explicit mass terms in the Lagrangian that appear after EWSB. Large radiative corrections to the Higgs mass arise from the hierarchy problem.

The mathematical framework of the SM is quantum field theory (QFT) which

merges quantum mechanics with special relativity. Using a Lagrangian formalism, the SM is composed of fields and interactions whose only allowed combinations are invariant under the transformations associated with global symmetries such as translation and rotation through space and, importantly, continuous local (gauge) transformations. As such, the SM is a chiral gauge theory under the symmetry group $SU(3)_C \times SU(2)_L \times U(1)_Y$.

Quantum electrodynamics (QED) describes, with unparalleled precision, the interactions of electrically charged particles and the electromagnetic field. The quarks and charged leptons carry a $U(1)_{EM}$ charge and participate in EM interactions which are mediated by the photon. QED is an Abelian theory whose effect is long range and decreases in strength with increasing distance.

Analogous to QED is quantum chromodynamics (QCD) which describes the strong interactions between quarks and gluons. The color $SU(3)$ gauge theory is non-Abelian resulting in a strong coupling constant that decreases at small distance scales. Consequently, the quarks behave essentially as free particles within hadrons, justifying the use of perturbation theory in the study of particle interactions at colliders where the particle interactions are at high momentum.

All the SM fermions participate in weak interactions which are mediated by the W^+ , W^- , and Z bosons, however a description of the weak sector does not follow a straight-forward analogy to QED or QCD. The fields of the quarks and leptons can be projected into their right- or left-components via the chiral projection operators^a

^aThe special properties of the γ^5 matrix are described in Section 2.2.

$P_{R,L} = (1 \pm \gamma^5)/2$. The left- and right-handed fermions transform differently under the $SU(2)_L \times U(1)_Y$ gauge group. Gauge invariance forbids explicit mass terms for all the gauge bosons and the fermions.

Electroweak (EW) theory, set forth by Glashow, Weinberg, and Salam [15, 16, 17], resolves these issues by showing that the weak and EM interactions emerge from the spontaneous symmetry breaking of an $SU(2)_L \times U(1)_Y$ gauge group. Above the EWSB scale ($\gtrsim 100$ GeV), gauge invariance under $SU(2)_L$ leads to the weak isospin triplet (W_1, W_2, W_3) , from which $W^\pm = (W_1 \mp W_2)/\sqrt{2}$, and to conservation of the third component of weak isospin T_3 . The B boson is the generator of $U(1)_Y$ symmetry that has conserved hypercharge Y associated with it. At lower energies, electroweak symmetry breaking via the Higgs mechanism results in an unbroken $U(1)_{EM} \subset SU(2)_L \times U(1)_Y$ which has conserved charge $Q = T_3 + Y/2$. The neutral B and W_3 bosons mix to form the mass eigenstates γ and Z :

$$\begin{pmatrix} \gamma \\ Z \end{pmatrix} = \begin{pmatrix} \cos \theta_W & \sin \theta_W \\ -\sin \theta_W & \cos \theta_W \end{pmatrix} \begin{pmatrix} B \\ W_3 \end{pmatrix} \quad (1.1)$$

where θ_W is the weak mixing angle which can be expressed in terms of the $SU(2)_L$ and $U(1)_Y$ couplings (g and g' , respectively) through $\cos \theta_W = g/\sqrt{g^2 + g'^2}$ and $\sin \theta_W = g'/\sqrt{g^2 + g'^2}$. The tree-level masses of the charged weak bosons W^+ and W^- relate to the mass of Z via $m_Z = m_W/\cos \theta_W$, while one massless vector boson remains — the photon. The weak force has a very short range, and its strength diminishes exponentially with distance.

In addition to generating mass terms for the gauge bosons, the Higgs mechanism generates mass terms for the quarks and charged leptons. The neutrinos remain massless in the SM, although neutrino oscillations require at least two of the three neutrino flavors to be massive.

The $SU(2)$ group has two base representations, a doublet and a singlet. The left-handed quarks and leptons are assigned to doublets of the $SU(2)$ gauge symmetry, while the right-handed components are assigned to the singlet states:

$$Q_L = \begin{pmatrix} u \\ d \end{pmatrix}_L, \quad L_L = \begin{pmatrix} \nu \\ e \end{pmatrix}_L, \quad u_R, \quad d_R, \quad e_R. \quad (1.2)$$

Note that there are no right-handed neutrinos in the SM. The W bosons couple to the left-handed doublets but not to the right-handed singlets.

While the Standard Model has made numerous predictions that have been experimentally confirmed to high precision, it still has its limitations. The values of the masses of the quarks, leptons, and Higgs boson, the strengths of the gauge couplings, and the angles of the Cabibbo-Kobayashi-Maskawa quark-mixing matrix are just some of the parameters whose values must be specified “by hand,” that is, defined by experiment and not by theory. Additionally, the SM does not include a description for gravity, nor does it explain the asymmetry of matter and anti-matter in the universe, or why there are three generations of quarks and leptons. These and other phenomenological and theoretical shortcomings lead physicists to investigate theories beyond the standard model.

1.2 Beyond the Standard Model

Because the SM provides no description of gravitation, dark matter, or neutrino masses, we know that it provides an incomplete picture of the universe. The SM is valid at the EWSB scale, but the laws of physics are unknown at much higher energy scales, such as the GUT scale ($\sim 10^{16}$ GeV) or the Planck Scale ($\sim 10^{19}$ GeV). For this reason the SM is an effective field theory, valid up to the EWSB scale and possibly higher, though how high is not known. To have a complete set of laws that govern particles and their interactions there must be UV completion, that is, a theory that describes physics up to the Planck scale. At some scale Λ , the new particles and interactions of the higher energy theory take effect, and at that point the effective field theory of the SM should match with the currently unknown high energy field theory.

How a parameter of a low energy effective field theory depends on the UV cutoff Λ determines its degree of UV sensitivity. The gauge and Yukawa couplings of the SM depend only logarithmically on Λ and as such are UV insensitive. However, a scalar mass-squared term, such as that of the Higgs boson, has corrections which scale as a positive power of the cutoff and is UV sensitive. We therefore expect the parameter to possess contributions proportional to Λ^2 . If the observed low-energy value of the parameter is not of the same order as the cutoff, there could be a few explanations. There could be an approximate symmetry in the limit where the parameter goes to zero. In this case, the parameter is said to “naturally” have a value significantly below the cutoff, since it is possible to envision scenarios where the symmetry-breaking effects

are naturally small. Alternatively, the parameter could simply be fine-tuned at the matching scale such that its value is much less than the cutoff, and this tuning cancels the large radiative corrections of the low energy theory. A theory with parameters that are all either UV insensitive (meaning, at worst logarithmically dependent on Λ) or whose UV sensitivity does not require tuning at the scale Λ is said to be natural.

The hierarchy problem stems from the large difference between the EWSB scale and the presumed scale of new physics. The observed Higgs boson mass m_H is ~ 125 GeV, and the Higgs mass-squared m_H^2 is subject to quadratically-divergent loop corrections from self-interactions, gauge loops, and fermion loops, particularly from the top quark:

$$\delta m_H^2 = \frac{\Lambda^2}{32\pi^2} \left[6\lambda + \frac{1}{4}(9g^2 + 3g'^2) - y_t^2 \right], \quad (1.3)$$

where λ is the Higgs self coupling and y^t is the top Yukawa coupling. Taking the cutoff Λ to be very large, perhaps near the GUT or the Planck scales, leads to quantum corrections much larger than the Higgs mass $\delta m_H^2 \gg m_H^2$. Apparently, the Higgs mass would naturally be at the scale of new physics, and yet this is not what is observed.

New physics entering at the TeV scale would greatly reduce the hierarchy problem and satisfy the requirements of naturalness by eliminating large loop corrections from above the TeV scale. Other outstanding questions can be addressed using new physics at the TeV scale. One particularly compelling motivation to search for new physics at the TeV scale is that of dark matter and the so-called ‘‘WIMP Miracle’’ which leads to thermal DM candidates [18, 19].

The SM does not describe *all* the matter or energy in the universe. In fact,

most of the energy content of the universe, 68.3% [3], is a form of energy ominously called dark energy. Dark energy is the reason the expansion of the universe is accelerating. The remaining 31.7% of the universe is composed of matter, but of this 84.5% (26.8% of the total energy content) is made up of what is known as dark matter. Only the remaining 4.9% of the energy content of the universe is made out of the baryonic matter described by the SM [3].

Although dark matter particles do not interact electromagnetically because of their abundance, DM has a significant impact on the large scale structure of the universe through gravitational interactions. In addition to being electrically neutral, any theorized DM particle candidate must be stable, long-lived, and non-relativistic. Candidate particles with a weak interaction cross section and weak-scale mass that satisfy these conditions are sometimes called WIMPs, short for Weakly Interacting Massive Particles [18, 19].

In the early universe, DM undergoes creation and annihilation reactions at equal rates when the temperature of the universe is much larger than the mass of the DM particle [18]. The creation and annihilation of DM slowed as the universe expanded and cooled down to a temperature below the DM mass. As the universe continued expanding, the density of DM was diluted until DM candidates no longer found each other, resulting in the relic abundance we see today. The predicted relic density for a DM candidate of mass \sim GeV-TeV with a cross section on a scale generic to weak interactions is approximately what is observed today. This WIMP miracle points to natural DM candidates which would have missing energy signals at a TeV scale particle

collider such as the LHC.

A number of classes of theories have been proposed to address these open questions in particle physics. Supersymmetry (SUSY) posits a new spacetime symmetry that requires that every SM particle have a corresponding supersymmetric partner particle, or sparticle, whose spin differs by 1/2. SUSY has mechanisms to resolve the aforementioned issues and more. For versions in which the sparticles have masses at the TeV scale, the contribution from the sparticles to loop corrections to m_H^2 cancel the large contributions from SM particles, thereby resolving the hierarchy problem.

A conserved multiplicative discrete symmetry of the SUSY Lagrangian called R-parity, where $R = (-1)^{3(B-L)+2S}$ for a particle of spin S with either baryon number B or lepton number L , is a feature of many SUSY models. SM particles are R-parity even, while their corresponding supersymmetric partners are odd under R-parity. Unbroken R-parity requires pair production of sparticles, and thus the lightest supersymmetric partner (LSP) is stable and cannot decay into SM particles. A neutral, weakly-interacting LSP from a particle spectrum in the GeV - TeV range makes an excellent DM candidate.

Another approach to solving the hierarchy problem is through Composite Higgs models [10, 11]. In these models, the Higgs boson is not an elementary scalar and is instead a pseudo-Goldstone boson of a global symmetry containing the electroweak group $SU(2)_L \times U(1)_Y$. The global symmetry is spontaneously broken by new strong dynamics at a higher scale. In generic composite Higgs models, the Higgs mass is protected by the shift symmetry, but this same shift symmetry has to be broken in order

to give the Higgs the required couplings to the gauge bosons, fermions, and itself. The Little Higgs scenario, one specific composite Higgs model, protects the shift symmetry by introducing new particles then requiring collective symmetry breaking [20, 21]. Some Little Higgs models also include an additional discrete symmetry called T-parity [22, 23]. Each particle of the theory has definite T-parity, and the lightest T-odd particle (LTP) is stable. This is frequently the B_H boson, the heavy partner to the photon. Because B_H is weakly interacting, it is a potential TeV-scale DM candidate.

Two more alternatives to solving the hierarchy problem are provided via extra dimensions (EDs). Introduced in 1998 by Arkani-Hamed, Dimopoulos, and Dvali, ADD or the large extra dimensions scenario posulates that the 3+1 dimensions of the SM are embedded into a space with two or more extra dimensions while allowing only gravity to propagate in the bulk [7, 8, 9]. Meanwhile, the SM fields are restricted to a (3+1)-dimensional brane. Generically for δ extra spatial dimensions with volume V_δ , the 4D Planck mass M_{Pl} is related to the fundamental $4+\delta$ -dimensional Planck mass $M_{(4+\delta)}$ by:

$$M_{Pl}^2 = M_{(4+\delta)}^{2+\delta} V_\delta. \quad (1.4)$$

If we take $M_{(4+\delta)}$ to be the fundamental mass scale, then the fundamental mass scale can be much smaller than the observed Planck mass, even down to the TeV scale, thereby eliminating the hierarchy problem.

Around the same time Randall and Sundrum (RS) proposed warped extra dimensions as another extra dimensional solution to the hierarchy problem [12]. The RS model proposes a 5D spacetime with a warped geometry that dilutes the effect of

gravity. Two branes are separated by the extra spatial dimension with coordinate z on an S^1/Z_2 orbifold with compactification radius r_c . The extra dimension spans the range $-\pi r_c \leq z \leq \pi r_c$ with the 4D branes located at the orbifold fixed points: the 4D “UV” or “Planck” brane is at $z = 0$, and the “IR” brane at πr_c . The space between the branes has a z -dependent metric:

$$ds^2 = e^{-2kr_c|z|} \eta_{\mu\nu} dx^\mu dx^\nu + r_c^2 dz^2, \quad (1.5)$$

where k is the scale parameter and x^μ are the coordinates for the usual four dimensions. The SM fields are confined to the visible IR brane. Consequently, the physical mass scales are set by a symmetry-breaking scale

$$v \equiv \exp(kr_c\pi)v_0 \quad (1.6)$$

which exponentially suppresses the mass scale v_0 of the hidden UV sector. In this case, the hierarchy problem is resolved by the exponential suppression in the visible sector of the high fundamental energy scales.

Both ADD and RS are theories of extra dimensions that propose dynamics testable at the LHC. A third theory of extra dimensions with dynamics at scales close to 1 TeV is Universal Extra Dimensions (UED) [13]. UED allows all SM field to propagate in one or more extra flat, compact dimensions. Whereas ADD and RS models aim to solve the hierarchy problem of the SM, motivations for UED models include the existence of a DM candidate particle [24, 25], the requirement of three fermion generations to cancel gauge anomalies [26], and proton stability [27].

As a simple extra dimensional extension of the standard model, UED provides prototype models to investigate constraints on EDs. The minimal form of UED (mUED) posits one extra spatial dimension through which all SM fields can propagate. While having only two free parameters, R^{-1} , the compactification scale of the single postulated extra dimension, and Λ , the high energy cutoff of the theory, mUED provides interesting phenomenology including a stable WIMP-type DM candidate that results from conservation of KK parity, analogous to R-parity in supersymmetry and T-parity in Little Higgs models.

Signatures of mUED at the LHC can be similar to signatures from other BSM theories, including SUSY and Little Higgs. All three models contain a conserved parity providing a stable WIMP-type dark matter candidates that exist at the TeV scale. Although dark matter particles cannot be directly detected in a particle accelerator, they would have a strong missing energy signature. After a two year technical stop, the LHC has just begun Run II, and is taking data at a center-of-mass energy of 13 TeV. If new heavy particles are discovered, we will need a precision measurement program at the LHC, because a linear collider, the usual purview of precision measurements, is many years away at best.

The goal of this dissertation is to present a prescription for ascertaining the precision with which a well-defined and predicted BSM coupling could be measured based on the observed number of events associated with a particular signature. At tree-level, the mUED strong coupling is the same as the SM strong coupling. For a given collider signature, varying the mUED strong coupling constant away from its predicted

value changes the number of mUED events expected with that signature. Bounds on the precision of a measurement of the mUED strong coupling are taken from the confidence bands of a plot of the varied mUED strong coupling vs. the number of expected mUED signal events. This number counting technique does not rely on measuring the cross sections of processes which make up the signature and therefore can accommodate cross sections with complicated dependences on powers of the coupling in question.

There are two potential uses for such a technique as applied here to mUED. If, at the time of implementation, the new particles were still open to multiple theoretical interpretations (such as if measuring particle spin had not yet been feasible), an analysis of the proposed kind could be utilized to favor or rule out mUED. Alternatively, if mUED were the dominant paradigm, one could follow the prescribed procedure for making a precision measurement of the mUED strong coupling in order to assess how well the model is performing.

A major advantage to this approach for precision measurements at the LHC is its generalizability. Future observations of new particles may not be consistent with mUED, but an analysis of this nature could be applied to other theories with couplings that have a well-defined relationship to the SM couplings. This technique can be used to perform a precision measurement of a coupling or disfavor a BSM theory under the challenging circumstances of a compressed mass spectrum and/or by using detector signatures that are composed of a signal process (or multiple processes, as in the mUED case) whose cross section relies on multiple couplings and therefore a precision measurement cannot be made from the simple relationship between a measured cross section

and the coupling of interest. Because the technique does not rely on this type of simple relationship but instead is a number counting experiment, the detector signature can be built up from a number of different processes, an advantage when measuring the coupling whose processes have individually small cross sections.

This dissertation is organized as follows: In Chapter 2, I present the theoretical background of Universal Extra Dimensions focusing on the minimal form of the theory. Chapter 3 details the methods and results of this precision measurement technique. Within this chapter, Section 3.1 provides a summary of the analysis scheme used. In Section 3.2, the technique for determining the precision measurement of the mUED strong coupling is described in detail for the parameter values $R^{-1} = 800$ GeV, $\Lambda R = 20$. In Section 3.3, this analysis is extended to cover the viable energy range 900 GeV $\leq R^{-1} \leq 1300$ GeV for $\Lambda R = 20$, and to the more condensed mass spectrum case of $R^{-1} = 800$ GeV with $\Lambda R = 5$. Finally, Chapter 4 concludes the description of this research and summarizes future directions for such a program. Appendix A lists relevant Feynman rules for mUED signal processes. Key statistical methods are discussed in Appendix B.

Chapter 2

Review of Universal Extra Dimensions

Modern theories with extra compact spatial dimensions (i.e., spatial dimensions of finite extent) have their origins in the 1920s with the development of Kaluza-Klein (KK) theory, an attempt to unify general relativity with electromagnetism [28, 29, 30]. To this end, KK theory was unsuccessful and lay more or less dormant until the 1980's when the need for extra dimensions (ED) in string theory prompted renewed interest in ED. Models such as those introduced in the late 1990's by Arkani-Hamed, Dimopoulos, and Dvali (ADD) [7, 8, 9], or Randall and Sundrum (RS) [12] provide mechanisms to address the hierarchy problem. The ADD model does this by postulating that the 3+1 dimensions of the SM are embedded into a space with two or more extra dimensions while allowing only gravity to propagate in the bulk. Alternatively, the RS model proposes a 5D spacetime with a warped geometry which dilutes the effect of gravity. By contrast, in 2001 Appelquist, Cheng, and Dobreanu advanced a theory known as Universal Extra Dimensions (UED) [13] which proposes one or more additional

flat spatial dimensions through which all SM fields can propagate, creating a Kaluza-Klein (KK) tower of particles for each of the corresponding SM particles. UED does not generally address the hierarchy problem (attempts are made in [31]), however other compelling motivations exist. Unlike ADD and RS which generically predict shorter proton lifetimes than are observed [32], six-dimensional models of UED limit higher dimensional operators that lead to proton decay, extending the proton lifetime beyond experimental bounds [27]. Six-dimensional UED models also provide a mechanism to derive the number of fermion generations from gauge anomaly cancellation [26]. With a TeV-scale mass spectrum and stable dark matter candidate, the lightest KK particle (LKP), five- and six-dimensional models of UED yield interesting phenomenology to investigate at the LHC.

2.1 General Features of UED

Characterized by one or more extra compact spatial dimensions on a flat metric which are accessible to *all* the SM fields, UED is a minimal extension of the SM in $d = 4 + \delta$ dimensions. The 4D effective field theory is valid below an energy scale Λ , above which the d -dimensional theory is no longer perturbative. The extra dimensions are compactified at the scale of the inverse radius of each extra dimension, $R^{-1} < \Lambda$. For any given δ and compactification scheme, the theory is completely parameterized by the size of the extra dimensions, the high energy cut-off of the theory, and by the boundary conditions of the extra dimensions.

One general feature of compact extra dimensions is the appearance of a KK tower in 4-dimensions corresponding to the d -dimensional field. A field propagating through compact extra dimensions gives rise to a set of 4D fields of different masses, each with the same spin. Each 4D field is referred to as a KK mode, KK excitation, or KK particle. A KK tower consists of the set of KK excitations corresponding to a single d -dimensional field. We find the KK tower when we integrate the d -dimensional Lagrangian density over the δ -dimensions to reduce the theory to a 4D effective theory. Take for example a massless 5D scalar field whose 5D Lagrangian density is [33]:

$$\mathcal{L}_5(x, y) = \frac{1}{2} \partial_M \Phi \partial^M \Phi = \frac{1}{2} (\partial_\mu \Phi \partial^\mu \Phi - \partial_y \Phi_n \partial_y \Phi_m) \quad (2.1)$$

where $\mu = 0, 1, 2, 3$ and y represents the coordinate of the fifth dimension. Assume the 5D field can be decomposed into factors dependent separately on the four Minkowski dimensions and the fifth dimension, $\Phi(x, y) = \sum_n \phi_n(x) \chi_n(y)$. Then the Lagrangian density can be rewritten as:

$$\mathcal{L}_5(x, y) = \frac{1}{2} \sum_{n,m} \left[\chi_n \chi_m \partial_\mu \phi_n \partial^\mu \phi_m - \phi_n \phi_m \partial_y \chi_n \partial_y \chi_m \right] \quad (2.2)$$

By setting conditions on the fields and how they behave at the boundaries of the extra dimension, we can simplify this double sum and elucidate the 4D effective theory. Let us assume the fields follow periodic boundary conditions and require the following two conditions:

$$\int_{y_1}^{y_2} dy \chi_n \chi_m = \delta_{nm} \quad (2.3)$$

$$\chi_m \partial_y \chi_n \Big|_{y_1}^{y_2} = 0 \quad (2.4)$$

The first condition, shown in (2.3), eliminates the double sum of (2.2) by requiring that the $\chi_n(y)$ form an orthonormal set. Additionally, we insist in (2.4) that the field or its fifth dimensional derivative vanishes at the boundaries.

Applying the conditions (2.3) - (2.4), then integrating the 5D Lagrangian density over y yields the 4D effective theory:

$$\mathcal{L}_{eff}(x, y) = \frac{1}{2} \sum_n \left[\partial_\mu \phi_n \partial^\mu \phi_n - m_n^2 \phi_n^2 \right] \quad (2.5)$$

This describes the KK tower, an infinite set of states. Each state or *mode* n has mass m_n . The masses observable in 4D correspond to quantized momenta in the fifth dimension.

In UED, the $n = 0$ modes of the KK towers are the SM fields. They are obtained from the 4D effective Lagrangian density by dimensional reduction of the $(4 + \delta)$ -dimensional Lagrangian density of UED. As in [13, 34], denoting the usual 3+1 non-compact spacetime coordinates as x^μ , $\mu = 0, 1, 2, 3$ and the coordinates of the compactified dimensions as y^a , $a = 1, \dots, \delta$, the $(4 + \delta)$ -dimensional Lagrangian density of UED is given by:

$$\begin{aligned} \mathcal{L}(x^\mu) = \int d^\delta y \left\{ - \sum_{i=1}^3 \frac{1}{2\hat{g}_i^2} \text{Tr} \left[F_i^{\alpha\beta}(x^\mu, y^a) F_{i\alpha\beta}(x^\mu, y^a) \right] + \mathcal{L}_{\text{Higgs}}(x^\mu, y^a) \right. \\ + i(\bar{Q}, \bar{u}, \bar{d}, \bar{L}, \bar{e})(x^\mu, y^a) (\Gamma^\mu D_\mu + \Gamma^{3+a} D_{3+a})(Q, u, d, L, e)(x^\mu, y^a) \\ + \left[\bar{Q}(x^\mu, y^a) \left(\hat{\lambda}_u u(x^\mu, y^a) i\sigma_2 H^*(x^\mu, y^a) + \hat{\lambda}_d d(x^\mu, y^a) H(x^\mu, y^a) \right) + \text{h.c.} \right] \\ \left. + \left[\bar{L}(x^\mu, y^a) \left(\hat{\lambda}_e e(x^\mu, y^a) H(x^\mu, y^a) \right) + \text{h.c.} \right] \right\} \quad (2.6) \end{aligned}$$

Here $F_i^{\alpha\beta}$ are the $(4 + \delta)$ -dimensional gauge field strengths of the $SU(3)_C \times SU(2)_L \times U(1)_Y$ gauge group. $D_\mu = \partial/\partial x^\mu - \mathcal{A}_\mu$ and $D_{3+a} = \partial/\partial y^a - \mathcal{A}_{3+a}$ are the covariant

derivatives with $\mathcal{A}_\alpha = -i \sum_{i=1}^3 \hat{g}_i \mathcal{A}_{\alpha i}^r T_i^r$ being the $(4 + \delta)$ -dimensional gauge fields, and \hat{g}_i the corresponding gauge couplings. These couplings as well as the $(4 + \delta)$ -dimensional couplings of the Yukawa matrices, λ_u , λ_d , and λ_e , have dimension $(\text{mass})^{-\delta/2}$. $\mathcal{L}_{\text{Higgs}}$ contains the kinetic term for the $(4 + \delta)$ -dimensional Higgs doublet, H , and the Higgs potential. Q , u , d , L , and e are the $(4 + \delta)$ -dimensional quarks and leptons whose zero-modes are described in the SM. Capital (lower case) letters correspond to fermion fields with the same quantum numbers as the SM $SU(2)_L$ doublets (singlets). Summation over fermion generations is implied.

The $(4 + \delta)$ -dimensional gamma matrices, Γ^α , are anti-commuting $2^{k+2} \times 2^{k+2}$ matrices, such that for an odd (even) number of compactified dimensions, $\delta = 2k$ ($\delta = 2k + 1$). These matrices satisfy the $(4 + \delta)$ -dimensional Clifford algebra $\{\Gamma^\alpha, \Gamma^\beta\} = 2g^{\alpha\beta}$. For an odd number of spacetime dimensions, construction of a matrix with the properties of γ^5 , that is a matrix which anticommutes with the Γ^M 's and whose square is the identity, is not possible. This leads to 2^{k+2} -component vector-like fermions in the case of odd extra dimensions as will be discussed below. Note that in the case of only one extra compact dimension, the gamma matrices can be expressed in terms of the usual 4-dimensional gamma matrices, $\Gamma_\mu = \gamma_\mu$ and $\Gamma_4 = i\gamma_5$.

To obtain the effective 4D Lagrangian from the $(4 + \delta)$ -dimensional Lagrangian density, the geometry of the compactification must be specified. Orbifold compactification, enforcing a discrete symmetry on the δ -dimensional manifold, is required to eliminate extra degrees of freedom which arise in the $n = 0$ mode but are not present in the SM. Consequentially, the chiral fermions of the SM can be obtained from the

vector-like fermions of the KK towers. Generally, the δ -dimensional space added to the usual $(3 + 1)$ -dimensional Minkowski space has coordinates $0 \leq y^a \leq \pi R$ for odd a and $-\pi R \leq y^a \leq \pi R$ for even a . Furthermore, fields propagating along the y^a coordinates are subject to boundary conditions of Eq. (2.4) such that each field or its derivatives with respect to the y^a 's vanish at the orbifold fixed points $y^a = 0, \pm\pi R$. Once the compactification scheme is in place, the field content of the $(4 + \delta)$ -dimensional theory can be specified. Orbifolding the extra dimensions breaks momentum conservation in the extra dimensions. However symmetries associated with the fixed points have associated conserved quantities which lead to interesting phenomenology.

2.2 Minimal UED

Minimal Universal Extra Dimensions (mUED), the focus of this work, is the simplest UED model and consists of only one extra dimension compactified on an S^1/Z_2 orbifold. mUED has only two free parameters: the size of the extra dimension R^{-1} and the cutoff scale of the theory Λ , commonly given as the dimensionless quantity ΛR , which counts the number of KK modes below the cutoff. A further assumption of mUED is that the boundary interactions of the 5D Lagrangian vanish simultaneously at the cutoff [14, 35].

Bounds on the size of the extra dimension depend on the cutoff energy. At the benchmark value of $\Lambda R = 20$, the viable range of the compactification scale is $720 \text{ GeV} \leq R^{-1} \leq 1350 \text{ GeV}$. A value of R^{-1} near the upper bound of this range is favorable for

dark matter relic density [3, 24, 36]; values above this bound lead to overclosure of the universe. The lower bound on R^{-1} was determined through collider experiments by the ATLAS Collaboration [37].

Higgs vacuum stability arguments [38, 39] motivate the consideration of a low ΛR scenario. The measured value of the Higgs boson implies that at some high energy, the potential for the Higgs boson develops a second minimum to which our universe could decay. The energy scale of this lower “true” vacuum depends sensitively on the masses of the Higgs boson and the top quark. Any viable BSM must require the lifetime of the universe’s decay to the true vacuum to be longer than the age of the universe. Because mUED introduces heavier versions of the top quark which couple strongly to the Higgs, the Higgs quartic coupling runs faster than in the SM resulting in a Higgs potential which goes to zero much faster than in the SM. Vacuum stability requires new physics to stabilize the observed vacuum thus constraining the upper limit of the cutoff to $\Lambda R \sim 5$. Although this argument for low ΛR is compelling, it has been shown that higher-dimensional operators associated with new physics at high energies may have a large effect on vacuum stability [40]. At $\Lambda R = 5$, the compactification scale is viable for $740 \text{ GeV} \leq R^{-1} \leq 1200 \text{ GeV}$, where again, the current lower bound is set by collider searches [41], while thermal dark matter relic density sets the bound from above [3, 24, 36].

The Z_2 symmetry of the orbifold breaks momentum conservation in the fifth dimension; however there still exists a conserved discrete symmetry called KK parity which is a remnant of the momentum conservation. All fields are required to be either

even or odd under the transformation $y \rightarrow -y$. This even or oddness is characterized by the conserved quantity $P_5 = (-1)^n$, where n is the n th mode of the KK tower. KK parity has a number of important consequences. First, requiring fields to have definite KK parity removes the unwanted extra degrees of freedom in the $n = 0$ KK excitation that are not present in the SM. Second, the $n = 1$ KK excitations have odd KK parity, therefore by KK parity conservation, the lightest KK particle (LKP) cannot decay to SM particles which have even KK parity.

Each 5D massless gauge field is made up of five $(\mathcal{A}_\mu, \mathcal{A}_5)$ components, each of which has an associated KK tower. By requiring the \mathcal{A}_μ (\mathcal{A}_5) to be even (odd) under KK parity, the $\mathcal{A}_{\mu,0}$ make up the components of a SM gauge boson, while $\mathcal{A}_{5,0}$ is eliminated from the theory, thus preventing the phenomenological problem of an undetected zero mode scalar field. For each $n \geq 1$ mode, a particular gauge choice (the unitary gauge) in which the $\mathcal{A}_{\mu,n}$ absorb the $\mathcal{A}_{5,n}$ through a Higgs-like mechanism. The $\mathcal{A}_{5,n}$ become the longitudinal polarization states of the massive \mathcal{A}_μ KK towers [42, 43, 44]. The Higgs doublet, H , must also be even under KK parity to ensure the appearance of the SM Higgs boson. The 5D gauge and Higgs bosons are decomposed into KK modes as follows:

$$\mathcal{A}_\mu^a(x^\mu, y) = \frac{1}{\sqrt{\pi R}} \left[\mathcal{A}_{\mu,0}^a(x_\mu) + \sqrt{2} \sum_{n=1}^{\infty} \mathcal{A}_{\mu,n}^a(x_\mu) \cos\left(\frac{ny}{R}\right) \right] \quad (2.7)$$

$$H(x^\mu, y) = \frac{1}{\sqrt{\pi R}} \left[H_0(x_\mu) + \sqrt{2} \sum_{n=1}^{\infty} H_n(x_\mu) \cos\left(\frac{ny}{R}\right) \right] \quad (2.8)$$

Here, \mathcal{A}_μ^a represents the $U(1)_Y$, $SU(2)_L$, $SU(3)_C$ gauge fields as in (2.6). The normalization reflects the range of integration $0 \leq y \leq \pi R$.

Because one cannot construct a 5-dimensional matrix with the properties of γ^5 , that is, a matrix whose square is the identity and that anticommutes with all the γ^μ , a single KK tower cannot give rise to fermions whose left and right-handed components transform differently with respect to $SU(2)_L$. This leads to vector-like fermions in 5D. Two KK towers of fields exist for each SM fermion, one, Ψ , which has the quantum numbers of the $SU(2)$ -doublet representation, and one, ψ , which has the quantum numbers of the $SU(2)$ -singlet representation. To eliminate the extra degrees of freedom introduced by doubling the number of fermions, use the usual 4D projection operators $P_L, P_R = \frac{1}{2}(1 \mp \gamma^5)$ and require $\Psi(x^\mu, y), \psi(x^\mu, y)$ to be even, odd under KK parity. The left and right-handed projections of the 5D fields are odd and even, respectively under the transformation $y \rightarrow -y$:

$$\Psi(x, y) = (P_L + P_R) \Psi(x, y) \xrightarrow{y \rightarrow -y} (-P_L + P_R) \Psi(x, -y) = \Psi(x, -y). \quad (2.9)$$

In this way, each factorized term in the tower is completely odd or completely even.

With the definite parity requirement, the fermionic towers take the form:

$$\begin{aligned} \Psi(x^\mu, y) = \frac{1}{\sqrt{\pi R}} & \left[P_L \Psi_0(x^\mu) + \sqrt{2} \sum_{n=1}^{\infty} \left(P_L \Psi_n^{(L)}(x^\mu) \cos\left(\frac{ny}{R}\right) \right. \right. \\ & \left. \left. + P_R \Psi_n^{(L)}(x^\mu) \sin\left(\frac{ny}{R}\right) \right) \right] \end{aligned} \quad (2.10)$$

$$\begin{aligned} \psi(x^\mu, y) = \frac{1}{\sqrt{\pi R}} & \left[P_R \psi_0(x^\mu) + \sqrt{2} \sum_{n=1}^{\infty} \left(P_L \psi_n^{(R)}(x^\mu) \cos\left(\frac{ny}{R}\right) \right. \right. \\ & \left. \left. + P_R \psi_n^{(R)}(x^\mu) \sin\left(\frac{ny}{R}\right) \right) \right]. \end{aligned} \quad (2.11)$$

Here Ψ represents the 5D fields with the same quantum numbers as Q or L , while ψ represents the 5D fields with the same quantum numbers as u, d , or e . The SM fermions

are given by $\Psi^{\text{SM}} = P_L \Psi_0 + P_R \psi_0$.

At tree level, the mUED mass spectrum is almost completely degenerate. The mass of each excitation of a KK tower associated with a SM particle X is approximately equal to the size of the extra dimension:

$$m_{X_n}^2 = \frac{n^2}{R^2} + m_{X_0}^2. \quad (2.12)$$

The zero mode mass m_{X_0} is the mass of the SM particle X and is generated via the Higgs mechanism. Radiative corrections lift the degeneracy of the mUED mass spectrum. Contributions to the KK masses include bulk corrections which arise from 5D Lorentz-violating corrections and from the renormalization of radiatively generated terms in the 5D Lagrangian which are localized at the boundaries (i.e., fixed points) of the orbifold. The combined mass corrections at one loop relevant to this work^a are those to the KK gluon g_1 , the KK $SU(2)$ doublet quarks Q_1 , the KK vector bosons W_1^\pm and Z_1 , the KK $SU(2)$ doublet leptons L_1 , and the KK photon γ_1 , the LKP [35]:

$$\begin{aligned} \delta(m_{B_n}^2) &= \frac{g_1^2}{16\pi^2 R^2} \left(\frac{-39}{2} \frac{\zeta(3)}{\pi^2} - \frac{n^2}{3} \ln \Lambda R \right) \\ \delta(m_{W_n}^2) &= \frac{g_2^2}{16\pi^2 R^2} \left(\frac{-5}{2} \frac{\zeta(3)}{\pi^2} + 15n^2 \ln \Lambda R \right) \\ \delta(m_{g_n}^2) &= \frac{g_3^2}{16\pi^2 R^2} \left(\frac{-3}{2} \frac{\zeta(3)}{\pi^2} + 23n^2 \ln \Lambda R \right) \\ \delta(m_{Q_n}) &= \frac{n}{16\pi^2 R} \left(6g_3^2 + \frac{27}{8}g_2^2 + \frac{1}{8}g_1^2 \right) \ln \Lambda R \\ \delta(m_{L_n}) &= \frac{n}{16\pi^2 R} \left(\frac{27}{8}g_2^2 + \frac{9}{8}g_1^2 \right) \ln \Lambda R, \end{aligned} \quad (2.13)$$

where $\zeta(3) \approx 1.2020\dots$ is the Riemann zeta function. With the radiative corrections,

^aFor the complete set of radiative mass corrections, see Refs. [34, 35].

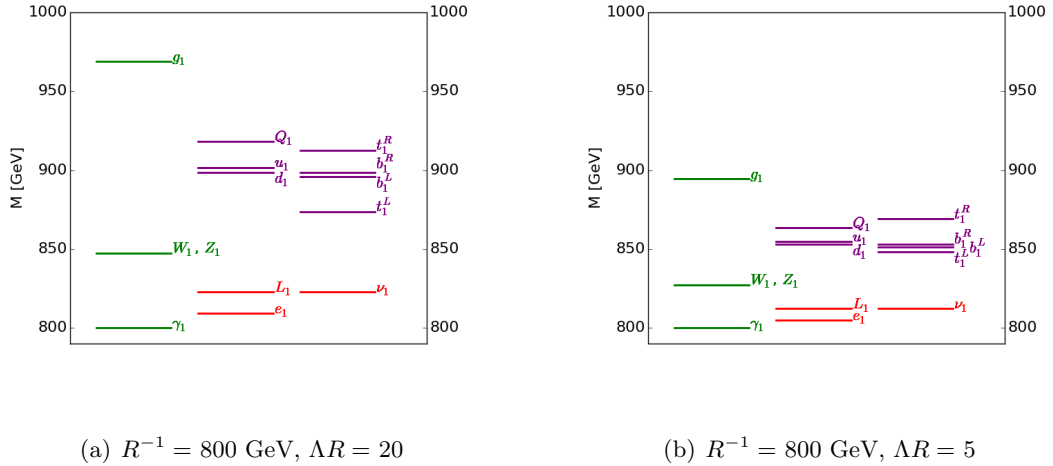


Figure 2.1: Mass spectra for the first KK level at one-loop for $R^{-1} = 800 \text{ GeV}$ for (a) $\Lambda R = 20$ and (b) $\Lambda R = 5$. Masses were computed using `CalcHEP-3.4.7` [45, 46].

the $\frac{n^2}{R^2}$ term in (2.12) is replaced by $\frac{n^2}{R^2} + \delta(m^2)$ for bosons and by $(\frac{n}{R} + \delta(m))^2$ for fermions. These substitutions are made in this way because the zero mode masses corresponding to the SM particles do not receive additional radiative corrections. All mass corrections are dependent on $\ln(\Lambda R)$ which leads to a more compressed spectrum for smaller values of ΛR than for a higher energy cutoff as can be seen in Fig 2.1.

With the small lifting of degeneracy, the KK particles can decay promptly via KK parity conserving interactions (see Fig 2.2). For the $n = 1$ mode, all KK particle interactions must occur in pairs. This leads to the stability of the LKP. In mUED for $R^{-1} \sim 1 \text{ TeV}$, the “Weinberg” mixing angle for the first level excitations is very small ($\sim 10^{-3}$) [35], so γ_1 is made up almost completely of B_1 , and has $m_{\gamma_1} \sim R^{-1}$. Because the LKP is a weakly interacting massive particle with a mass detectable at the LHC, γ_1 makes an interesting dark matter candidate.

Another notable feature of mUED is that the couplings for the SM particles

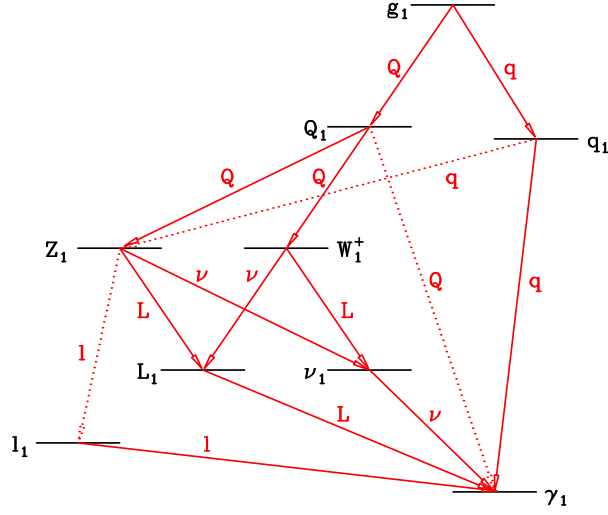


Figure 2.2: The $n = 1$ KK decay chain. Solid lines represent the dominant transitions. Taken from Ref. [14].

are the same for all modes within a KK tower. Of particular interest to this work is the strong coupling (referred to as g_3 in (2.12), simply called g going forward). At tree-level, the strong coupling associated with $n \geq 1$ modes is predicted to be the same as that for the SM:

$$g_{sm}(qqg) = g_{sm}(Q_1 Q_1 g) = g_{ued}(q Q_1 g_1). \quad (2.14)$$

This relationship gives a straightforward prediction for the mUED strong coupling that is testable at the LHC. The next chapter describes a technique for determining how precisely the mUED strong coupling could be measured at the LHC.

Chapter 3

Precision Measurement at the LHC

3.1 Analysis Scheme

The investigation into the precision with which one can measure the mUED strong coupling relies on the following assumptions: 1) New particles consistent with mUED have been discovered at the LHC. 2) The masses of these particles, particularly in the g_1 and Q_1 cascade decays, have been determined. 3) The LHC has been running at its design center-of-mass energy^a, 14 TeV, and 4) the integrated luminosity is $\geq 100 \text{ fb}^{-1}$.

The proton-proton collisions at the LHC generate an abundance of KK gluons and KK quarks. The largest production cross sections yield a collider signature of jets plus missing energy, which, unfortunately has large SM background arising from Z +jets, W^\pm +jets, $t\bar{t}$, and QCD backgrounds contributions. To minimize the SM background,

^aWhile these simulations were run assuming the LHC design energy of 14 TeV, the next LHC run is scheduled to have a center-of-mass energy of 13 TeV. This energy is high enough that the mUED processes described in this paper will still be within reach at the LHC.

we first considered a monojet signal in the vein of Ref. [47]. This signature requires the production of a KK quark with a KK vector boson, and the production cross section combined with the relatively compressed mass spectrum of mUED did not produce enough high transverse momentum monojets in excess of the SM background to make the precision measurement.

Alternatively, because KK gluons and KK quarks frequently produce leptons during their cascade decays, selecting for like-sign dilepton events, which have a relatively smaller SM background at the LHC, provides an attractive signal to use for investigating mUED. In this analysis, I look for an excess number of like-sign dilepton events over the expected number of Standard Model events of the signal of interest:

$$pp \rightarrow l^\pm l^\pm + \text{jets} + \cancel{E}_T \quad (3.1)$$

where $l = e$ or μ , and there are two or more jets in addition to missing energy.

If mUED correctly describes the newly discovered particles, then by Eq. (2.14) $g_{ued}/g_{sm} \propto 1$, and for specific values of R^{-1} and ΛR there is an associated number of signal events, S_1 , expected to be produced at the LHC. However if the ratio of the mUED and SM strong couplings is not necessarily unity but instead $g_{ued}/g_{sm} = c$, where c is some constant value, then a different number of signal events, S_c , is expected to be produced at the LHC. This variation of the coupling away from the predicted value is similar to the “ κ -framework” used to explore the coupling structure of a Higgs-like particle at the LHC [48]. For each estimate S_c , a profile likelihood calculator is used to find the central confidence intervals with 68.3% and 95.4% coverage. The profile

likelihood calculator requires two trials of every event simulation, one to construct a model of the likelihood, and one to supply the “observed” number of events. To test how precisely g_{ued} can be measured, one varies this ratio of the mUED and SM strong couplings away from unity and evaluate how this variation changes the ratio κ :

$$\kappa = \frac{S_c}{S_1}, \quad (3.2)$$

The bounds on the precision of a g_{ued} measurement are taken from the confidence bands of the plot of g_{ued}/g_{sm} vs. κ , where for a given measurement of κ , there is a range of possible values of g_{ued} consistent with that measurement.

If the spins of the new particles have not been identified, then there could be multiple theoretical interpretations [14]. In this case, the strong coupling of the new particles may not be the mUED strong coupling but rather an unknown BSM strong coupling. The technique for determining the precision measurement of g_{ued} could be used to eliminate mUED as the correct interpretation. For ease of notation, the strong coupling of the new particles will be referred to as g_{ued} , although it could be the coupling of an alternative theory such as SUSY [14].

3.2 Precision measurement of UED strong coupling

The demonstration of this technique for assessing the precision measurement of the mUED strong coupling focuses on the parameter values $R^{-1} = 800$ GeV, $\Lambda R = 20$. This scenario is just above the current lower bound of the size of the extra dimension while using the benchmark value for the cutoff. This value provides the best

Decay	BR	Comments
$g_1 \rightarrow q, Q_1$	40%	$q \neq t, Q_1 \neq T_1$
$Q_1 \rightarrow q, W_1$	65%	$Q_1 \neq T_1$
$Q_1 \rightarrow q, Z_1$	32%	$Q_1 \neq T_1$
$W_1 \rightarrow l, \nu, \gamma_1$	78%	$l = e, \mu$; decays went through either L_1 or ν_1
$Z_1 \rightarrow l^+, l^-, \gamma_1$	39%	$l = e, \mu$; decays went through L_1

Table 3.1: Relevant branching ratios for mUED scenario: $R^{-1} = 800$ GeV and $\Lambda R = 20$. Branching ratios were computed using `CalcHEP-3.4.7` [45, 46]. In all cases the SM quarks q and KK quarks Q_1 are not SM or KK top quarks. The KK leptons (charged and neutral) decay exclusively to SM leptons and the LKP.

representation of the utility of the technique by balancing the size of the cross section with the compression of the mass spectrum. Relevant masses and branching ratios for this scenario are shown in Fig. 2.1(a) and Table 3.1 respectively.

3.2.1 Kaluza-Klein quark and gluon production at the LHC

To investigate the mUED strong coupling, consider subprocesses involving first level KK gluons g_1 and SU(2) doublet quarks Q_1 :

$$\begin{aligned}
qq &\rightarrow Q_1 g_1 \\
qq &\rightarrow Q_1 Q_1 \\
qq &\rightarrow g_1 g_1 \\
gg &\rightarrow Q_1 Q_1,
\end{aligned} \tag{3.3}$$

examples of which are shown in Figs. 3.1 and 3.2^b. These processes all involve one or more KK gluons and have cross sections proportional to g_{ued}^2 , g_{ued}^3 , g_{ued}^4 , or some linear combination of these factors. If the cross sections of the hard processes were directly proportional to some unique power of g_{ued} , I could make an estimate of the precision measurement of g_{ued} using the signal uncertainty as in Refs. [47, 49, 50]. However, the mixture of powers of g_{ued} makes this approach intractable. Because the technique to assess the possible precision of the measurement of g_{ued} described here relies only on the number of events of the given signal and not on the cross section of a particular process, I am free to investigate a signal made up of different processes. This approach has the benefit of evaluating the precision measurement of the coupling even though the cross sections of the signal have complicated dependences on g_{ued} . I therefore follow the number counting technique described in this section.

Due to the mass hierarchy of the $n = 1$ KK modes, g_1 and Q_1 will cascade decay through the KK vector bosons, Z_1 and W_1^\pm , leading to final states with Standard Model quarks and leptons as well as missing energy:

$$\begin{aligned}
Q_1 &\rightarrow q + W_1 \rightarrow \text{jet} + l + \cancel{E}_T \\
Q_1 &\rightarrow q + Z_1 \rightarrow \text{jet} + l^+ l^- + \cancel{E}_T, \quad \text{where one lepton is lost} \\
g_1 &\rightarrow q + Q_1 \rightarrow 2 \text{ jets} + l + \cancel{E}_T, \\
g_1 &\rightarrow q + Q_1 \rightarrow 2 \text{ jets} + l^+ l^- + \cancel{E}_T, \quad \text{where one lepton is lost}
\end{aligned} \tag{3.4}$$

The mUED signal is defined as all subprocesses of the form given in Eq. (3.3) that

^bFeynman rules applicable to mUED signal processes are given in Appendix A.

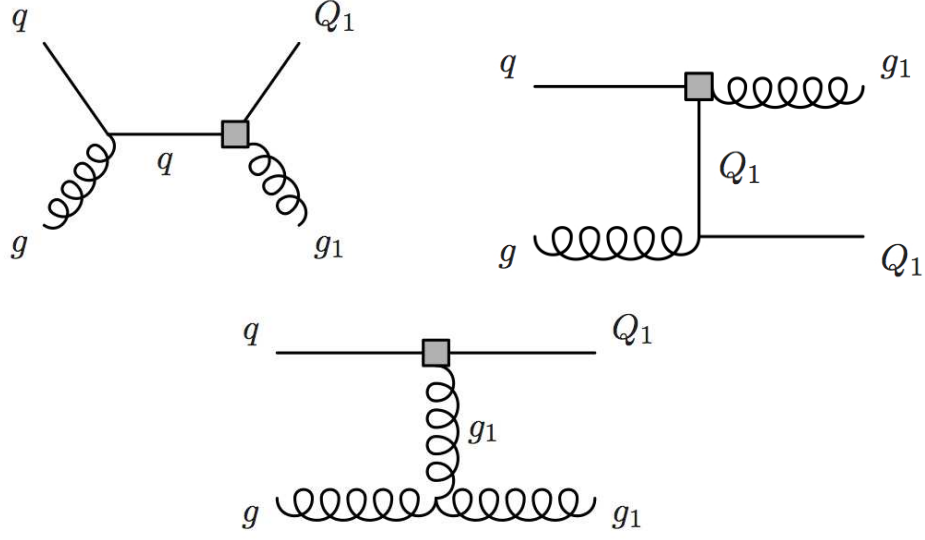


Figure 3.1: Diagrams for $qq \rightarrow Q_1g_1$, the process which yields the largest contribution to the signal cross section. The g_{ued} coupling appears at the boxed vertices. Note that $\sigma_{Q_1g_1} \propto g_{ued}^2$.

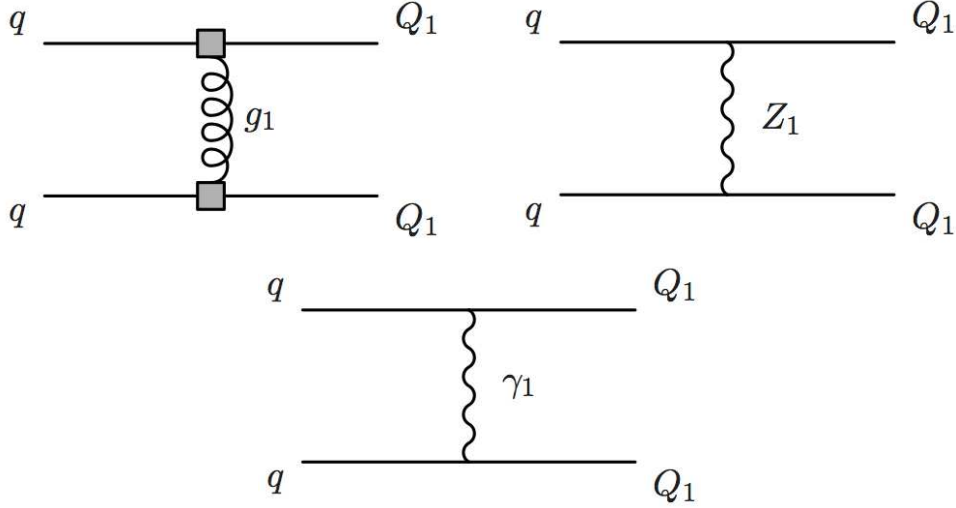


Figure 3.2: Diagrams for $qq \rightarrow Q_1Q_1$, the process which yields the second largest contribution to the signal cross section. The g_{ued} coupling appears at the boxed vertices. Note that $\sigma_{Q_1Q_1} \propto c_1 + c_2g_{ued}^2 + c_3g_{ued}^4$. In this case, some diagrams do not contain the mUED strong coupling, however the $c_2g_{ued}^2$ and $c_3g_{ued}^4$ terms account for $> 90\%$ of the cross section of this process.

contain at least one qQ_1g_1 vertex and proceed through the decays shown in Eq. (3.4) that result in the signal of interest —exactly two like-sign leptons, two or more hard jets, and missing energy in the final state.

3.2.2 Major Backgrounds and Signal Selection

Signal and background samples were simulated in pp collisions at a center-of-mass energy of 14 TeV. The mUED signal and background tree-level matrix elements and KK cascade decays were generated using mUED model files^c[46] within CalcHEP-3.4.7 [45], and were subsequently interfaced with Herwig++-2.7.0 [52] for showering and hadronization. For consistency with the $t\bar{t}$ background, the simulations were run with the CT10nlo [53] parameterization of the parton distribution function (PDF) using LHAPDF [54]. The Herwig++ output was analyzed using HepMC-2.06.01 [55] and ROOT [56]. Electrons and muons with $p_T > 5$ GeV were considered isolated if no more than 10 GeV was inside a cone of radius $\Delta R = \sqrt{\Delta\phi^2 + \Delta\eta^2} = 0.2$ around the lepton momentum, where ϕ and η are the azimuthal angle and pseudorapidity respectively. Jets were identified using fastjet-2.4.2 [57, 58], where I employed the anti-kT jet clustering algorithm [59] with $\Delta R = 0.7$ and required each jet to have $p_T > 30$ GeV.

To find the number of signal events for varying g_{ued}/g_{sm} , I customized the mUED model files by varying the strong coupling associated with the qQ_1g_1 vertex according to $g_{ued}/g_{sm} = c$, for $c = (0.7, 0.8, \dots, 1.2, 1.3)$, while fixing the particle masses

^cAlthough a more recent set of mUED model files [51] were produced in 2012, the structure of the model files created by Cheng, Matchev, and Schmaltz, provided the needed flexibility in the treatment of the mUED strong coupling and masses, which depend directly on g_{ued} [35].

at the values generated with the unchanged strong coupling ($c = 1$). I fix the masses at their predicted values because of the assumption that the masses of the particles observed at the LHC are consistent with the particle spectrum for mUED. Fixing the masses prevents additional changes to the mUED cross sections via the mass corrections given in Eq. (2.13). I then generated the hard processes in `CalcHEP` and continued the event simulation as described above.

There are two types of backgrounds to the signal processes: SM and mUED. The SM background is dominated by semileptonic $t\bar{t}$ decay with a smaller but non-negligible contribution from $W^\pm W^\pm jj$. The $t\bar{t}$ events were generated to next-to-leading order in α_S via `POWHEG` [60, 61, 62, 63], while $W^\pm W^\pm jj$ processes were generated at tree-level with `MadGraph5-v1.5.10` [64]. The CT10nlo parameterization of the PDF was used in implementing both SM backgrounds. Event files were then run through `Herwig++` and analyzed as described above.

All mUED processes that were not identified as signal were considered as mUED background. The mUED background was produced simultaneously with the signal events as previously noted. All possible first level KK processes were produced and allowed to cascade decay.

mUED production cross sections, branching ratios and masses were taken from the `CalcHEP` simulations. Signal process cross sections decrease significantly as R^{-1} increases as shown in Fig. 3.3. For ΛR fixed at 20, the cross section for all processes contributing to the mUED signal for $R^{-1} = 1200$ GeV is less than 10% that of $R^{-1} = 800$ GeV. The $t\bar{t}$ and $W^\pm W^\pm jj$ cross sections were taken from `POWHEG` and `MadGraph5`

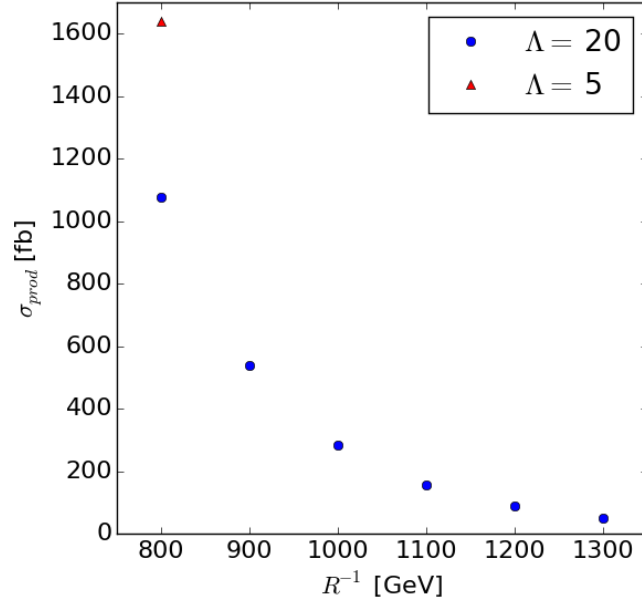


Figure 3.3: mUED signal cross sections as a function of R^{-1} . Cross sections were computed using CalcHEP-3.4.7 [45, 46]

respectively.

Because the mUED signal is characterized by two like-sign leptons, two or more jets, and missing energy, the signal was selected by following the cutflow shown below and in Table 3.2.

- Anticipated trigger: $p_{T,l1} > 25$ GeV, $p_{T,j1} > 100$ GeV, $\cancel{E}_T > 100$ GeV
- Exactly two isolated like-sign leptons: ee , $\mu\mu$, or $e\mu$, as long as both leptons have the same charge
- Two hard jets: $p_{T,j1} > 200$ GeV, $p_{T,j2} > 100$ GeV
- Missing energy: $\cancel{E}_T > 250$ GeV

cut	SM bkg.	mUED bkg.	signal	S/\sqrt{B}
events generated	8.24×10^7	1.83×10^6	107,700	11.7
trigger	4.29×10^6	365,000	21,900	10.2
like-sign leptons	60,900	786	4,980	20.1
2 hard jets	16300	171	1,220	9.5
missing p_T	1310	101	810	21.6
max lepton p_T	508	91	721	29.5
b -tag veto	162	90	714	45.0

Table 3.2: Cutflow for mUED scenario: $R^{-1} = 800$ GeV and $\Lambda R = 20$, with assumed integrated luminosity of 100 fb^{-1} at center-of-mass energy $\sqrt{s} = 14$ TeV. Trigger cuts demand $p_{T,l1} > 25$ GeV, $p_{T,j1} > 100$ GeV, $\cancel{E}_T > 100$ GeV. The SM background is composed of $t\bar{t}$ and $WWjj$ events. All other SM backgrounds are negligible.

- Maximum lepton momentum: $p_{T,l1} < 60$ GeV
- b -jet veto: tagging efficiency of $\epsilon = 70\%$, light quark mistag rate of $D = 1\%$ [65, 66]

These cuts are optimized for S/\sqrt{B} for the $R^{-1} = 800$ GeV, $\Lambda R = 20$ scenario. I implemented the first four cuts to select the signal of interest. The compressed mass spectrum of mUED limits the transverse momentum of the final state particles. Making these cuts aggressive enough to adequately reduce the $t\bar{t}$ background sacrifices the mUED signal events. The final two cuts were applied to further reduce the substantial $t\bar{t}$ background. A cut on the maximum value for the transverse momentum of the hardest lepton was implemented because the tail of the $t\bar{t}$ distribution of hardest lepton's p_T extends well beyond that of the mUED signal as shown in Fig. 3.4. The b -jet veto effectively increases

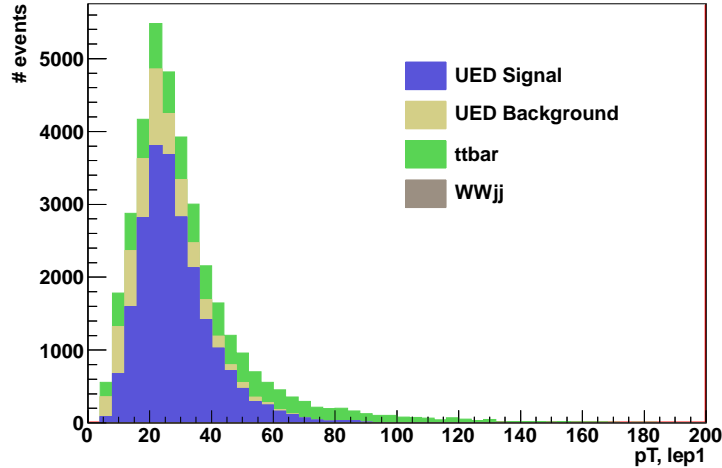


Figure 3.4: Distribution of p_T of the hardest lepton of events with exactly two like-sign leptons for mUED scenario: $R^{-1} = 800$ GeV, $\Lambda R = 20$. There are too few $WWjj$ events too be seen in the histogram.

S/\sqrt{B} because only approximately 3% of the mUED signal contains events with b -jets. The working point of 70% efficiency with a mistag rate of 1% was chosed to optimize S/\sqrt{B} . These simple cuts reduced both the SM and mUED background to levels such that $S/\sqrt{B} \geq 14$ for an extra dimension as large as $R^{-1} = 1100$ GeV with $\Lambda R = 20$.

Although for this pilot study I did not implement a detector simulation, I estimated the detector effects by smearing the momenta of the final state particles using a Gaussian function before applying cuts. For example, to test how sensitive the lepton momentum is to the lepton trigger cut and the maximum lepton p_T cut, I smeared the p_T of the hardest lepton with a Gaussian function with a mean of 1 and with a variance of 10%. I then observed the change in the number of events passing cuts. I found that the number of events that passed cuts were insensitive to cut values,

and the resulting change to the bounds on g_{ued} were negligible.

3.2.3 Sources of mUED signal uncertainty

The systematic signal uncertainty is as shown in Table 3.3. All errors were added in quadrature. The error in the luminosity is specified by the LHC [67, 68]. I determined the CT10nlo PDF uncertainty using the Hessian technique as recommended by the CTEQ collaboration [69, 70, 71]. The NLO uncertainty was obtained by varying the renormalization scale Q around the central value Q_0 as $\frac{1}{2}Q_0 \leq Q \leq 2Q_0$, where $Q_0 = \sqrt{2stu/(s^2 + t^2 + u^2)}$ and taking the maximum percent discrepancy of the number of signal events. The author is not aware of any studies done to assess how precisely the first level KK masses or R^{-1} could be measured at the LHC. For this reason, I estimated the uncertainty associated with the mass measurements of g_1 , Q_1 , and γ_1 by assuming the masses associated with these particles are known to within a benchmark value of ± 10 GeV (assuming that masses can be measured as precisely as predicted for certain SUSY scenarios [72]), then ran simulations with the masses adjusted accordingly and took the largest percentage change in the number of signal events as the systematic signal uncertainty associated with the uncertainty of the KK masses.

The current assessment of the systematic error gives a total systematic signal uncertainty of 64%, a value too high to conduct the analysis at hand. If new particles are discovered over the next few years, it is reasonable to expect a diminution of the individual sources of uncertainty such that the total systematic uncertainty of the signal may be reduced to within 10-30%. At the present time, the uncertainties due to PDF

error	$\Delta S/S$
luminosity	3.0%
PDF uncertainty	38.1%
NLO corrections	34.0%
$\Delta m_{KK} = 10$ GeV	38.4%
total	64.0%

Table 3.3: Current assessment of relative errors of number of signal events for mUED scenario: $R^{-1} = 800$ GeV and $\Lambda R = 20$ with assumed integrated luminosity of 100 fb^{-1} at $\sqrt{s} = 14$ TeV. Errors were added in quadrature. All uncertainties except that due to luminosity are expected to decrease by the time the LHC reaches 100 fb^{-1} .

uncertainty, NLO corrections, and KK particle mass uncertainty are all comparable to each other. The large PDF uncertainty can likely be attributed to the combination of the low fractional momentum of the incoming quarks and high momentum transfer of the pp collisions at the LHC [73]. Once the LHC has been running at its design energy long enough to reach 100 fb^{-1} , PDFs will certainly be better constrained at 14 GeV. Improvements to NLO corrections are also expected: if mUED candidate particles had been discovered, then loop corrections to the mUED processes will have been calculated. The signal uncertainty associated with the precision of the masses may be harder to reduce. Due to the compressed mass spectrum of mUED, small changes in mass can significantly restrict the energy available to decay particles yielding a large change in the number of signal events that pass cuts. Particle masses will need to be measured with greater sensitivity to alleviate this source of error.

3.2.4 Bounds on the g_{ued} measurement

To determine the bounds on the precision with which one can measure g_{ued} , I ran full event simulations for $g_{ued}/g_{sm} = c$, with $c = 0.7, 0.8, \dots, 1.2, 1.3$, and observed the effect on κ , the number of signal events for a given c relative to the number of signal events for $c = 1$. The upper and lower bounds on κ were found by employing a profile likelihood calculator, based on the results described in Ref. [74], implemented in the `Roostats` [75] framework of `ROOT`. The bounds on g_{ued} were extracted by plotting the confidence intervals associated with κ as in Fig. 3.5.

The profile likelihood calculator builds a model based on the expected numbers of mUED signal and total background events, following Poisson distributions, and their associated Gaussian-distributed systematic uncertainties. A sample data set is then constructed as the total “observed” number of events. Using the method of maximum likelihood, the calculator estimates the number of expected signal events S and its lower and upper bounds for central confidence intervals with 68.3% and 95.4% coverage. I ran two complete simulation trials for each value of c , then used the two trials to build the model (trial 1) and supply the “observed” data set (trial 2).

At the present time, the systematic uncertainty on the signal is 64%, however, as discussed above, this is expected to be largely reduced by the time an experimental analysis of this type is undertaken. In the calculator, I used more optimistic estimates of the signal uncertainty: 10%, 20%, and 30%. The major source of background events is $t\bar{t}$, which currently has an estimated combined scale and PDF cross section uncertainty

of $\sim 12\%$ as calculated by the **Hathor** tool [76]. Cross sections derived at next-to-next-to-leading order in Ref. [77] reduce the uncertainty to 4–6%. The background uncertainty is assigned at the benchmark value of 10% in all cases, as the current uncertainty on the major background source is expected to be reduced by the time the LHC reaches 100^{-1} fb.

Fig. 3.5 shows the correlation between κ and the coupling ratio for $R^{-1} = 800$ GeV and $\Lambda R = 20$, with an assumed integrated luminosity of 100 fb^{-1} at $\sqrt{s} = 14$ TeV. A measurement at the LHC of $\kappa = 1$ would correspond to an observation of the number of signal events expected for mUED in which $g_{ued} = g_{sm}$. For an optimistic scenario of a 10% systematic signal uncertainty, a $\kappa = 1$ measurement would indicate that g_{ued} falls somewhere within $\pm 7\%$ of its predicted value to 95.4% confidence level (CL). More conservatively, if the systematic signal uncertainty is as high as 30%, the same observation would imply that g_{ued} could lie anywhere between -20% and $+13\%$ of its predicted value, again to 95.4% CL. Alternatively, if κ were observed to be a value other than one, one could use the relationship between g_{ued}/g_{sm} and κ to determine whether or not the number of events observed are consistent with mUED to 68.3% or 95.4% CL. For example, an observation of $\kappa = 0.75$ would still be consistent with mUED for a systematic signal uncertainty of 20% or 30%, however, if the systematic signal uncertainty is brought down as low as 10%, an observation of $\kappa = 0.75$ would no longer be consistent with mUED to 95.4% C.L.

3.3 Results of precision measurement of strong coupling

The technique for determining the possible precision which which the mUED strong coupling could be measured at the LHC as described above was used to scan the viable range of R^{-1} : $900 \leq R^{-1} \leq 1300$ GeV in 100 GeV increments for the cutoff $\Lambda R = 20$. Because the masses of the KK particles scale with R^{-1} , this parameter scan provides insight into how heavier mass spectra affect the bounds on the precision measurement of g_{ued} . Whereas R^{-1} controls the scale of the mass spectrum of KK particles, both R^{-1} and ΛR control the compression of the spectrum. The bounds for $R^{-1} = 800$ GeV with $\Lambda R = 5$ were therefore also assessed in order to investigate the case of a very compressed mass spectrum. Results for the full range of R^{-1} at $\Lambda R = 20$ and $R^{-1} = 800$ GeV with cutoff $\Lambda R = 5$ with assumed integrated luminosity of 100 fb^{-1} are shown in Figs. 3.5 - 3.11. The complete bounds on a precision measurement of g_{ued} are given in Tables 3.4 and 3.5.

As R^{-1} increases, we generally see a relaxation on the bounds on the possible precision of a g_{ued} measurement for the fixed cutoff $\Lambda R = 20$. The mass differences between KK parent and daughter particles in the decay chains (cf. Eq. (3.4) and Fig. 2.2) increase with larger R^{-1} , giving rise to harder jets and leptons and larger transverse missing energy in the final state. However, this advantage is in tension with the decrease in the production cross sections associated with the heavier mass spectra (cf. Fig. 3.3).

Using this technique of varying the mUED to SM strong coupling ratio, upper and lower bounds were set at 95.4% C.L. on the precision with which the g_{ued} coupling

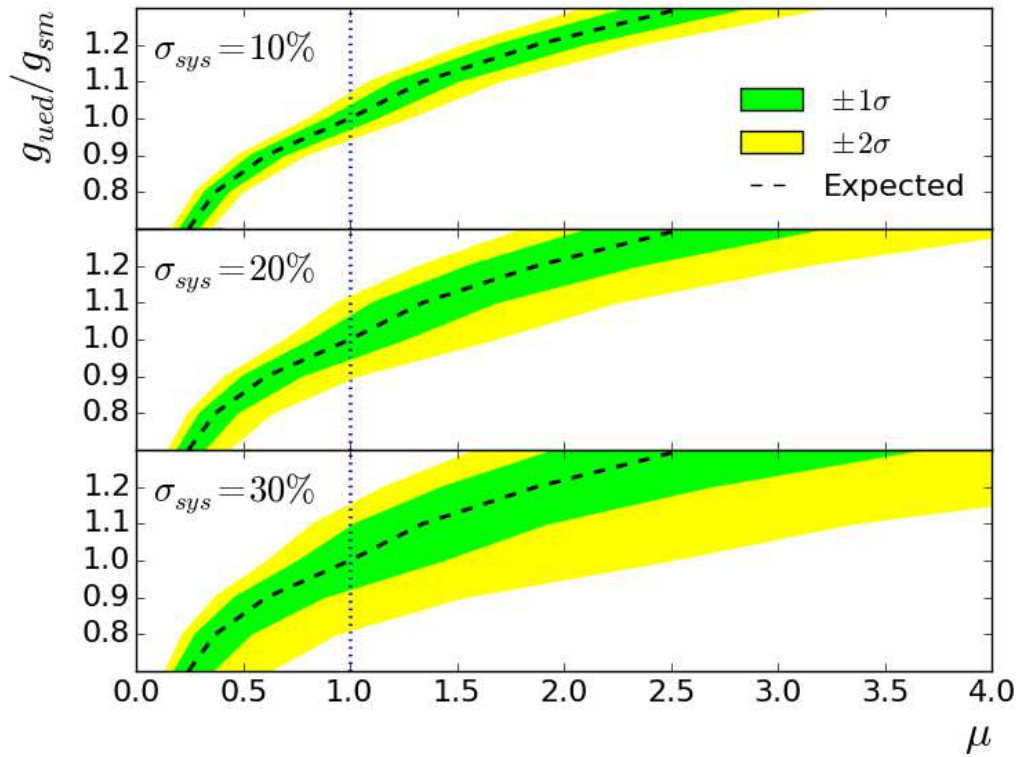


Figure 3.5: g_{ued}/g_{sm} vs. κ for $R^{-1} = 800$ GeV with $\Lambda R = 20$. The assumed integrated luminosity is 100 fb^{-1} at $\sqrt{s} = 14$ TeV.

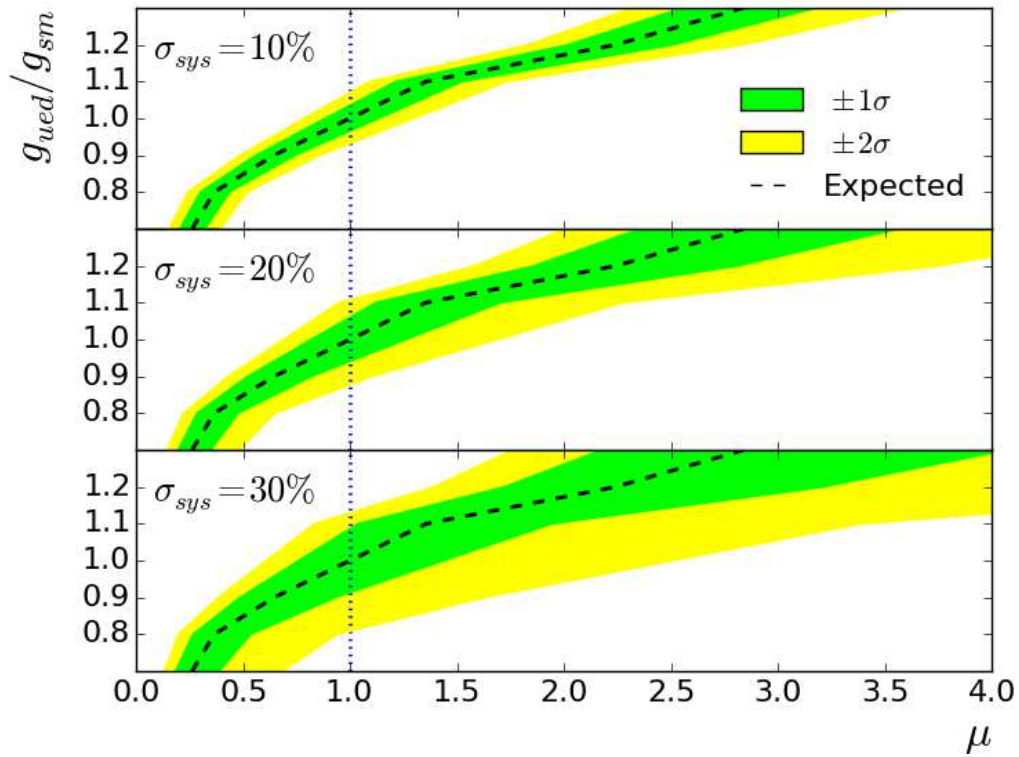


Figure 3.6: g_{ued}/g_{sm} vs. κ for $R^{-1} = 900$ GeV with $\Lambda R = 20$. The assumed integrated luminosity is 100 fb^{-1} at $\sqrt{s} = 14$ TeV.

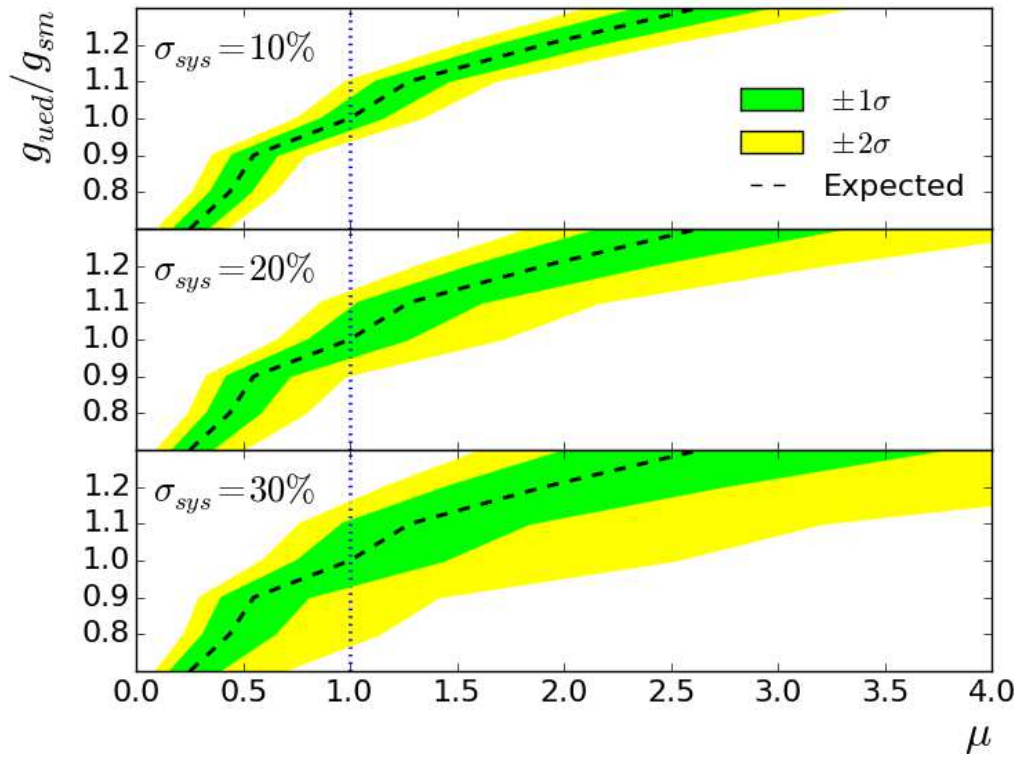


Figure 3.7: g_{ued}/g_{sm} vs. κ for $R^{-1} = 1000$ GeV with $\Lambda R = 20$. The assumed integrated luminosity is 100 fb^{-1} at $\sqrt{s} = 14$ TeV.

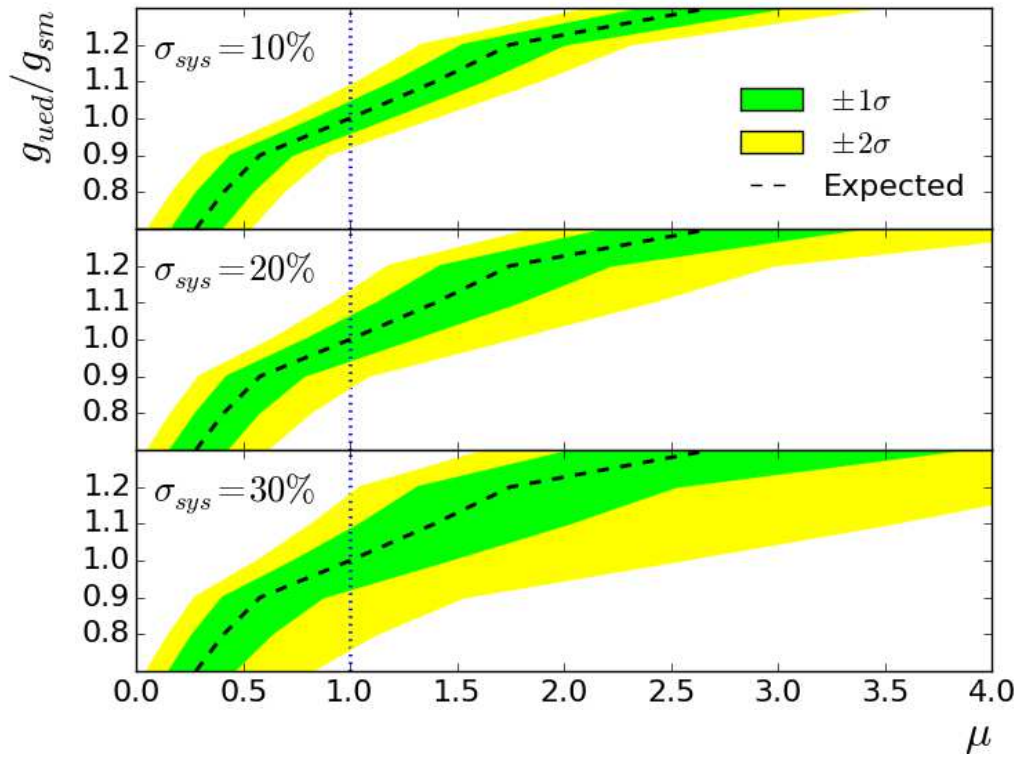


Figure 3.8: g_{ued}/g_{sm} vs. κ for $R^{-1} = 1100$ GeV with $\Lambda R = 20$. The assumed integrated luminosity is 100 fb^{-1} at $\sqrt{s} = 14$ TeV.

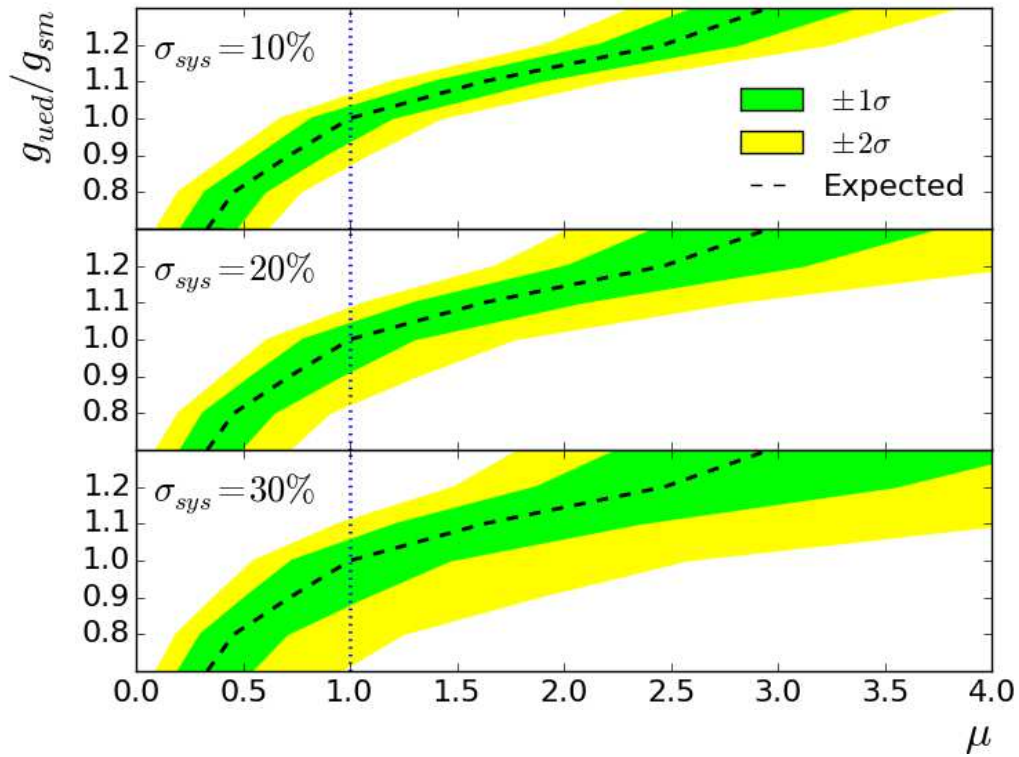


Figure 3.9: g_{ued}/g_{sm} vs. κ for $R^{-1} = 1200$ GeV with $\Lambda R = 20$. The assumed integrated luminosity is 100 fb^{-1} at $\sqrt{s} = 14$ TeV.

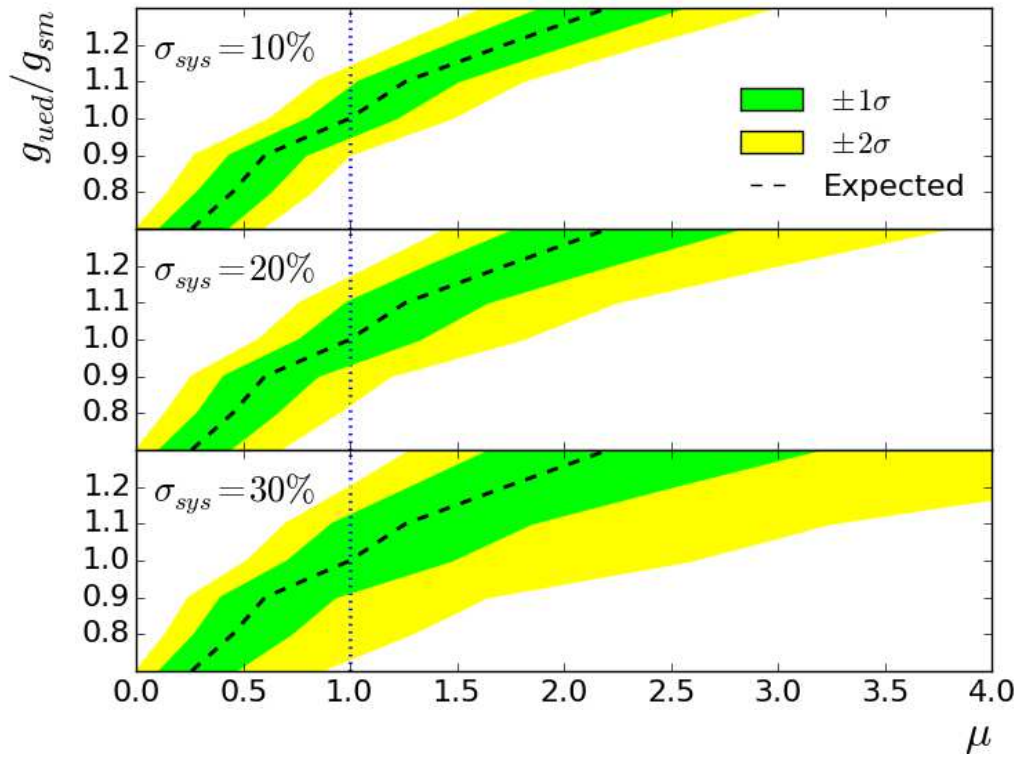


Figure 3.10: g_{ued}/g_{sm} vs. κ for $R^{-1} = 1300$ GeV with $\Lambda R = 20$. The assumed integrated luminosity is 100 fb^{-1} at $\sqrt{s} = 14$ TeV.

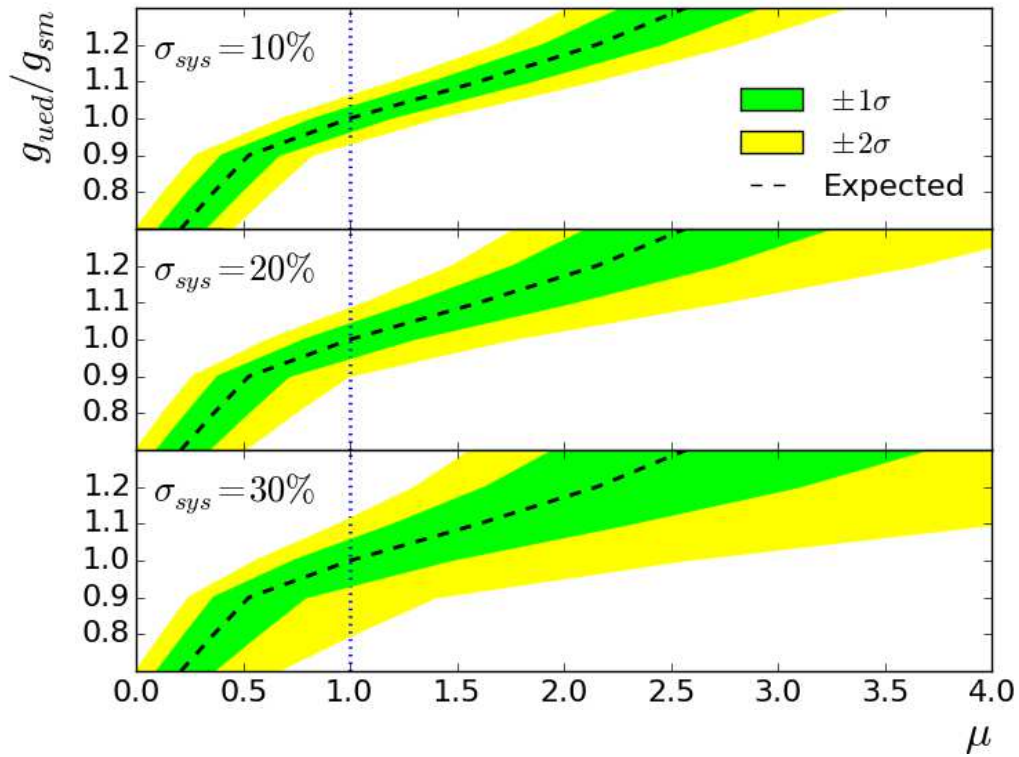


Figure 3.11: g_{ued}/g_{sm} vs. μ for $R^{-1} = 800$ GeV with $\Lambda R = 5$. The assumed integrated luminosity is 100 fb^{-1} at $\sqrt{s} = 14$ TeV.

R^{-1} (GeV)	ΛR	Sig. unc.	-2σ	-1σ	$+1\sigma$	$+2\sigma$
800	20	10%	0.943	0.971	1.033	1.067
		20%	0.892	0.947	1.061	1.114
		30%	0.810	0.922	1.090	1.151
900	20	10%	0.932	0.965	1.035	1.070
		20%	0.877	0.940	1.060	1.108
		30%	0.809	0.913	1.087	1.130
1000	20	10%	0.939	0.969	1.052	1.103
		20%	0.903	0.951	1.083	1.130
		30%	0.769	0.930	1.107	1.159
1100	20	10%	0.921	0.960	1.043	1.088
		20%	0.869	0.943	1.061	1.129
		30%	0.758	0.921	1.084	1.178

Table 3.4: Bounds on g_{ued}/g_{sm} for $R^{-1} = 800, 900, 1000,$ and 1100 GeV, $\Lambda R = 20$ with assumed integrated luminosity of 100 fb^{-1} at $\sqrt{s} = 14$ TeV. Systematic background uncertainty is 10% in all cases.

R^{-1} (GeV)	ΛR	Sig. unc.	-2σ	-1σ	$+1\sigma$	$+2\sigma$
1200	20	10%	0.873	0.937	1.031	1.062
		20%	0.823	0.912	1.042	1.084
		30%	0.714	0.880	1.055	1.110
1300	20	10%	0.900	0.948	1.082	1.139
		20%	0.822	0.931	1.104	1.168
		30%	0.732	0.912	1.122	1.200
800	5	10%	0.931	0.964	1.029	1.060
		20%	0.901	0.949	1.041	1.083
		30%	0.795	0.931	1.056	1.113

Table 3.5: Bounds on g_{ued}/g_{sm} for $R^{-1} = 1200$ and 1300 GeV, $\Lambda R = 20$ and for $R^{-1} = 800$ GeV, $\Lambda R = 5$ with assumed integrated luminosity of 100 fb^{-1} at $\sqrt{s} = 14$ TeV. Systematic background uncertainty is 10% in all cases.

could be determined for the viable range of compactification scale at $\Lambda R = 20$ and for the lower ΛR test case for all three tested values of the systematic signal uncertainty. The bounds for all points in the parameter scan except for $R^{-1} = 1200$ and 1300 GeV were determined using cuts optimized for the test scenario $R^{-1} = 800$ GeV, $\Lambda R = 20$. Because the transverse momenta of the final state leptons, jets and invisible particles increases with R^{-1} , reoptimizing the cuts for the higher values of the compactification scale, $R^{-1} = 1200$ and 1300 GeV, was required to set bounds at 95.4% C.L. The only change in the cutflow was to the missing transverse energy cut which required $\cancel{E}_T > 300$ GeV instead of 250 GeV.

For fixed R^{-1} , lower values of ΛR yield a more compressed mass spectrum, with the mass of the LKP essentially unchanged. This results in significantly lighter KK quarks and gluons, leading to a large increase in the production cross sections of the processes of interest. For $R^{-1} = 800$ GeV, the signal production cross section increased by over 50% for $\Lambda R = 5$ compared to $\Lambda R = 20$. The more tightly compressed mass spectrum also restricts the momenta of the outgoing leptons, jets, and invisible particles. For $R^{-1} = 800$ GeV, S/\sqrt{B} was reduced from 45.0 for $\Lambda R = 20$ to 13.1 for $\Lambda R = 5$.

The biggest limitation of this technique as applied to the mUED signature of two like-sign leptons, two or more jets, and missing energy is the reduction of the signal to background ratio for larger values of R^{-1} or smaller value of ΛR . The compressed mass spectra of the mUED scenarios make it difficult to severely reduce the $t\bar{t}$ background through these simple selection cuts. For example, the hardest leptons coming from $t\bar{t}$ decays are likely those coming from the subsequent $W \rightarrow l\nu$ decays, in which

the charged lepton and neutrino have negligible mass compared to the W , so that the mass difference is $\Delta m_{W,lv} \approx 80$ GeV. For the mUED decays, the mass difference in the $W_1 \rightarrow lL_1$ decays is only $\Delta m_{W_1, lL_1} \approx 25$ GeV for $R^{-1} = 800$ GeV, $\Lambda R = 20$ and only $\Delta m_{W_1, L_1} \approx 34$ GeV for the less compressed spectrum of $R^{-1} = 1200$ GeV, $\Lambda R = 20$.

A first approach to boosting signal and reducing the $t\bar{t}$ background would be to optimize event selection cuts for each point in the mUED parameter space. Implementing a more sophisticated set of cuts is also likely to improve the precision measurement. The $t\bar{t}$ events which pass event selection cuts can be sensitive to the choice of PDF. In this study, the $t\bar{t}$ simulations employed the CT10nlo PDF for consistency with the choice of PDF for mUED events. However, when $t\bar{t}$ events were simulated using the MSTW2008nlo PDF [78], the production cross section was higher, but the number of events which passed selection cuts was significantly lower, yielding much tighter bounds on g_{ued} . Constraining the PDFs at higher energies will have a substantial impact on the size of the $t\bar{t}$ background in the future.

The current size of $t\bar{t}$ background causes the systematic background uncertainty to dominate over the statistical uncertainty; thus, increasing the luminosity to 300 fb^{-1} or 3000 fb^{-1} yields only marginal improvement on the precision measurement. The $t\bar{t}$ background will need to be reduced in order for increased statistics to improve the result.

Chapter 4

Conclusion

In this dissertation I have presented a method for determining how precisely a well-defined coupling of a theory could be measured at the LHC assuming that new particles had been discovered and their masses had been characterized. As applied to the strong coupling of mUED, this technique is viable for the full parameter range $800 \text{ GeV} \leq R^{-1} \leq 1300 \text{ GeV}$, $\Lambda R = 20$ and for the low ΛR test case of $R^{-1} = 800 \text{ GeV}$, $\Lambda R = 5$ as observed at the LHC with a center-of-mass energy of 14 TeV (and presumably the current run at $\sqrt{s} = 13 \text{ TeV}$) and integrated luminosity of 100 fb^{-1} . If an experimental measurement of the excess number of events over the background of the signature of two like-sign leptons with two or more jets and missing energy falls near $\kappa = 1$ as defined in Eq. 3.2, then the maximal precision of the measurement of g_{ued}/g_{sm} corresponds to the upper and lower bounds of the confidence bands of Figs. 3.5 - 3.11 associated with the measured value of κ . If the number of signal events were to lie above or below $\kappa = 1$, then it may be possible to exclude mUED as the appropriate theory to

describe the particles to 68.3% and/or 95.4% C.L., as the measured coupling would not be consistent with mUED.

Improvements to the possible precision measurement of the mUED strong coupling could be made with a reduction of SM background. Future results from the design-energy run of the LHC, including better tuning of PDFs for $t\bar{t}$ and for mUED processes will help in reducing the systematic uncertainty of both signal and background contributions to the event signature. The signature events in this analysis were selected using a set of simple cuts. To perform this analysis on data generated from the LHC, a more sophisticated set of criteria for event selection would be prudent to achieve a larger signal to background ratio.

A useful extension to this analysis would be the inclusion of a third lepton in the collider signature. This would bolster the signal as well as decrease the $t\bar{t}$ background if a suitable cut on the third lepton is made.

An analysis of this type would be augmented by a complementary study investigating processes that rely on different branching ratios within mUED, for example, processes involving the production and decay of KK $SU(2)$ -singlet quarks q_1 within mUED. The dominant decay of q_1 is $q_1 \rightarrow q + \gamma_1$, which means that for events in which two q_1 are directly produced from parton-parton interactions or from a decaying g_1 , the resulting signature would be two or more jets plus large missing energy. If the formidable SM background of Z +jets, W^\pm +jets, $t\bar{t}$, and QCD background can be reduced, then applying the described method for assessing how precisely g_{ued} could be determined would indicate the robustness of the technique.

Non-minimal forms of UED also present interesting and rich particle spectra. For instance, one may consider non-vanishing bulk masses and boundary localized terms [79]. Alternatively, embedding the mUED model in a larger space with N additional dimensions of $\mathcal{O}(eV^{-1})$, accessible only to gravity [80] and a $(4+N)$ -dimensional Planck scale can result in prompt decay of the LKP: $\gamma_1 \rightarrow \gamma + G$, where G is a tower of graviton states, with mass between 0 and R^{-1} . The ATLAS collaboration is currently conducting searches for this model [81] and have set the lower 95% CL limit on R^{-1} at 1.4 TeV.

The prime benefit of the method presented here is its generalizability. Unlike other approaches to assessing the precision with which a coupling may be measured, which rely on a direct relationship between the process cross section and the coupling (such as $\sigma \propto g^2$), the technique can be applied to processes whose cross sections have complicated dependences on the coupling. This allows for measurements of couplings via a BSM signature that is composed of a collection of processes whose combined events can be seen in aggregate against the SM background. Because this approach is general, the technique can be applied to other versions of UED or other BSM theories with predicted SM-like couplings.

Appendix A

Select Feynman Rules for mUED

Below is a list of Feynman rules needed to compute scattering amplitudes of the mUED signal processes (cf. Eq. (3.3)) and the subsequent two-body decays within the resulting cascade decay chains. Vertices shown in Table A.1 contain the strong coupling, here denoted as g_3 . These vertices are needed for the production of $SU(2)$ -doublet KK quarks and KK gluons, and for the decay of a KK gluon into a $SU(2)$ -doublet KK quark. Vertices shown in Table A.2 contain either the weak coupling g_2 or the electromagnetic coupling g_1 . These vertices appear in the decay chains starting from the $SU(2)$ -doublet KK quark.

These Feynman rules were derived in [46] from the compactified 5-dimensional Lagrangian given in Eq. (2.6) after dimensional reduction. All processes are KK-parity conserving and given in terms of 4-dimensional fields.

$$= -ig_3 f^{abc} [(p-q)_\lambda g_{\mu\nu} + (q-r)_\mu g_{\lambda\nu} + (r-p)_\nu g_{\lambda\mu}]$$

$$= -ig_3 \gamma^\mu T_{ba}^c P_L$$

Table A.1: Feynman rules for colored particles. The f^{abc} are the structure constants for $SU(3)_c$. $g_{\mu\nu}$ is the 4D metric tensor $(+, -, -, -)$. The left-handed projection operator is represented as $P_L = \frac{1-\gamma^5}{2}$.

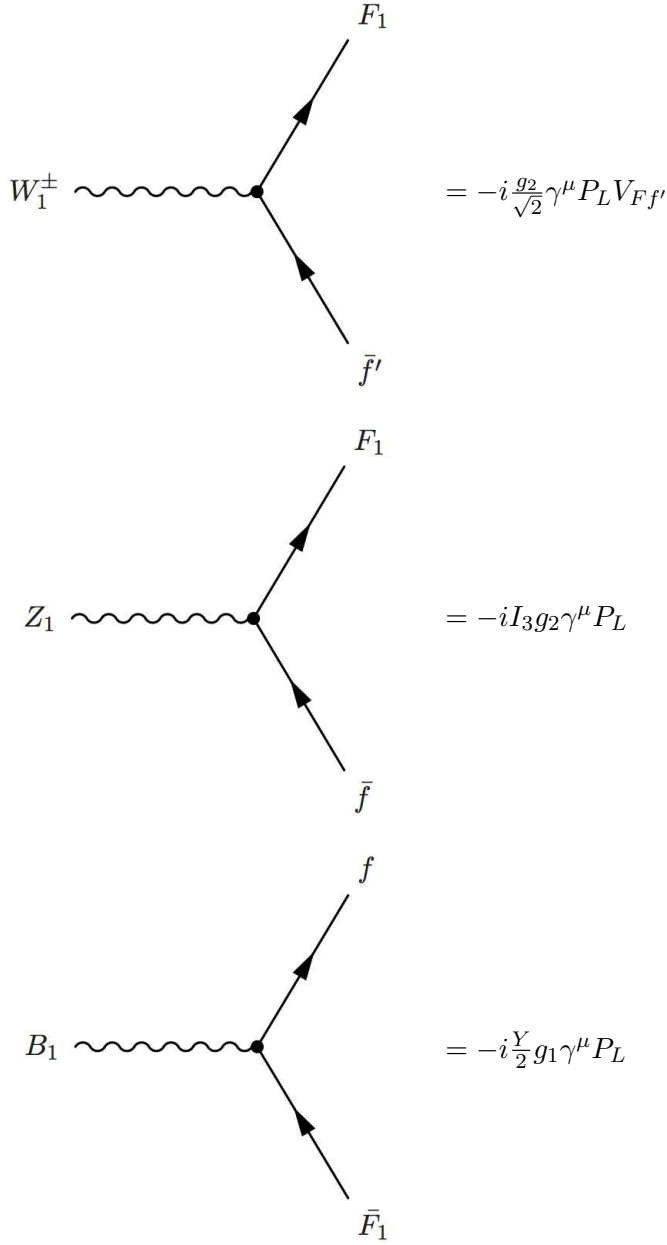


Table A.2: Feynman rules for weakly and electromagnetically interacting particles. f and F_1 represent SM and $n = 1$ KK $SU(2)$ fermions respectively. I_3 is the weak isospin. Y stands in for the fermion hypercharges. The left-handed projection operator is represented as $P_L = \frac{1-\gamma^5}{2}$.

Appendix B

Statistical Methods

The outcomes of particle physics experiments are non-deterministic. We use the data gathered from an experiment, or, as in this case, a simulated experiment, usually given as a random sample from a large set, to statistically infer properties of a given probabilistic model. The technique developed in this dissertation relies on estimating the number of mUED signal-type events detected at the LHC and assessing the uncertainty of this estimate. The uncertainty of this estimate depends not only on the statistical fluctuations of the signal but also on the number of background events and the systematic uncertainties of both the signal and background. The estimate for the number of signal events was performed in two trials using Monte Carlo methods. The estimate for the confidence intervals for the signal, here the range of possible values of the signal in which the true value of the signal lies with a probability of 68.3% or 95.4%, was determined via the profile likelihood ratio, an extension of the Method of Maximum Likelihood. Additionally, Bayesian statistics were employed to test the consistency of

the results from the Monte Carlo trials. These statistical methods are discussed below, following a review of key concepts needed for their discussion.

Key concepts of parameter estimation

To discuss the methods of parameter estimation employed in this analysis, some background in probability and statistics is needed. Of particular importance are the concepts of probability and probability distributions, random variables, statistical tests, and parameter estimation.

Consider the sample space S which consists of the set of all possible outcomes of a particular experiment, and denote $A, B \subseteq S$ are any pair of events. For any subset (i.e., outcome) such as A of S , one assigns the probability $P(A)$ that A will occur. The real number $P(A)$ must satisfy the following three axioms:

$$\begin{aligned} P(A) &\geq 0, \\ P(A \cup B) &= P(A) + P(B) \text{ if } A \cap B = \emptyset, \\ P(S) &= 1. \end{aligned} \tag{B.1}$$

A number of other properties can be derived from these axioms (see, e.g., Refs. [82, 83]).

The probability of outcome A given outcome B , known as the conditional probability $P(A|B)$ is (assuming $P(B) \neq 0$):

$$P(A|B) = \frac{P(A \cap B)}{P(B)}. \tag{B.2}$$

Likewise, assuming $P(A) \neq 0$, the probability of B given A is:

$$P(B|A) = \frac{P(B \cap A)}{P(A)}. \quad (\text{B.3})$$

Since $A \cap B = B \cap A$, Eqs. (B.2) and (B.3) combine to form:

$$P(A|B) = \frac{P(B|A)P(A)}{P(B)}, \quad (\text{B.4})$$

an equation known as Bayes' theorem.

When a probability distribution is specified on the sample space of the experiment, the probabilities of all the possible outcomes must sum to one. The outcomes of experiments can be expressed in different ways so long as their probabilities follow the axioms of Eq. (B.1). A random variable x is a function that maps each possible outcome $s \subset S$ a real number $x(s)$. With a probability distribution specified on the sample space of the experiment, the probability distribution for the possible values of any random variable x can be determined.

The purpose of a statistical test is to determine the compatibility of the observed data with the hypothesized probabilities. Generally, the hypothesis specifies a probability distribution $f(x; \boldsymbol{\theta})$ for the random variable x , where the distribution has a defined form and is dependent on a limited number of free parameters $\boldsymbol{\theta} = (\theta_1, \dots, \theta_m)$. When $f(x_i; \boldsymbol{\theta})$ is taken to be a function of the parameters $\boldsymbol{\theta}$ with the data x_i fixed, this factor is called the likelihood function L :

$$L(\boldsymbol{\theta}) = \prod_{i=1}^n f(x_i; \boldsymbol{\theta}). \quad (\text{B.5})$$

To investigate the agreement between data and theory, one constructs a test statistic $t(x)$ a random variable that can be used to distinguish between alternative hypotheses.

The goal of parameter estimation is to find the estimate of the parameters that best describe the data. A statistic used to estimate a parameter θ is called an estimator. To characterize how “good” an estimator is, consider a few of its properties. An estimator is said to be consistent if as the sample size increases the estimate approaches the true value of the parameter. The bias of an estimator is the difference between the expectation value of the estimator and the true value of the parameter, and an estimator is called unbiased if this difference is zero. An estimator is said to be efficient if the variance of the estimator, $V[\theta]$, is equal to the Rao-Cramer-Frechet bound:

$$V[\theta] = \left(1 + \frac{\partial b}{\partial \theta}\right) / E \left[- \frac{\partial^2 \log L}{\partial \theta^2} \right]. \quad (\text{B.6})$$

If the likelihood depends on more than one unbiased and efficient parameter, the inverse of the covariance matrix of their estimators $V_{ij} = \text{cov}[\theta_i \theta_j]$ is

$$(V^{-1})_{ij} = E \left[- \frac{\partial^2 \log L}{\partial \theta_i \partial \theta_j} \right]. \quad (\text{B.7})$$

This technique can be used to find the variance of an estimator (each diagonal element of V_{ij} gives the variance of a particular parameter), even if the parameter was estimated using a method other than maximum likelihood.

B.1 Method of Maximum Likelihood

The goal of the analysis described in this work was to determine how precisely the mUED strong coupling, g_{ued} , could be measured at the LHC for the energy range. To do this, I varied the strength of g_{ued} and observed how this changed s , the predicted

number of events in excess of the predicted background for the signature of interest. Then, by finding the confidence intervals in which the probability of finding the true value of s is 68.3% or 95.4%, I created confidence bands for g_{ued}/g_{sm} vs. κ , where κ is the number of signal events for the value of g_{ued}/g_{sm} modulo the number of signal events for $g_{ued} = g_{sm}$ as seen in Figs. 3.5 - 3.9. I predicted s and the number of background events b using Monte Carlo simulations. To find the confidence intervals for s while incorporating the systematic uncertainties of the mUED signal and total background, I employed the method of maximum likelihood as implemented in the `RooStats` [75] package of `ROOT` [56], based on the results described in [74]. This approach identifies the confidence intervals with the desired coverage by taking as input a representative data set, called the Asimov data set, defined such that when one uses it to evaluate the estimators for all parameters, one obtain the true parameter values [74]. One generates estimates for the true parameter values from a Monte Carlo model using a very large data sample. One then applies the method of maximum likelihood in the form of the profile likelihood ratio which treats the number of background events as well as the systematic uncertainties of the signal and background as nuisance parameters.

The functional form of the probability distribution for a random variable is often known (or at least a well-motivated prediction of the form can be made), but the parameters of the distribution may not be. For example, the number of events n observed in counting experiments in particle physics follow a Poisson probability

distribution with mean and variance ν :

$$P(n|\nu) = \frac{\nu^n}{n!} e^{-\nu}. \quad (\text{B.8})$$

The parameter ν is unknown, and the goal in the counting experiment is to estimate this parameter given the data n .

The method of maximum likelihood is a powerful technique for parameter estimation used frequently in particle physics. When the functional form of the probability distribution for a random variable is known, but the parameters $\boldsymbol{\theta}$ are not, one may maximize the likelihood for the unknown parameters to obtain the maximum likelihood estimators of the distribution. Given a differentiable likelihood function, as in Eq. (B.5), the best estimators $\hat{\boldsymbol{\theta}} = \hat{\theta}_1, \dots, \hat{\theta}_m$ of the unknown parameters are determined by maximizing the likelihood for each parameter:

$$\frac{\partial L}{\partial \theta_i} = 0, \quad i = 1, \dots, m. \quad (\text{B.9})$$

The likelihood function for this analysis is the product of the distributions that describe the number of events observed in the experiment and the distributions for the systematic uncertainties of the signal and background events.

Often the parameters of the likelihood can be separated into two categories: parameters of interest and nuisance parameters. The nuisance parameters are parameters of the model which cannot be eliminated from the model but are nevertheless not the focus of the experiment.

Generally, when the likelihood is a function of a single parameter of interest π and of nuisance parameters θ_i the maximum likelihood estimators (MLE's) are given

by:

$$(\hat{\pi}, \hat{\theta}_i) = \operatorname{argmax}_{\pi, \theta_i} L(\pi, \theta_i) \quad (\text{B.10})$$

Unlike the likelihood, the profile likelihood, $L(\pi, \hat{\theta}_\pi)$ is a function of only the parameter of interest (and the subscript i has been dropped for convenience). The profile likelihood is constructed by first estimating each nuisance parameter by treating the parameter of interest π as being fixed to some value (indicated by the subscript π):

$$\hat{\theta}_\pi = \operatorname{argmax}_{\theta} L_\pi(\theta) \quad (\text{B.11})$$

This procedure is repeated so there is one curve L_π for each value of π . Note that because $\hat{\theta}_\pi$ is a function only of the parameter π , the profile likelihood $L(\pi, \hat{\theta}_\pi)$ is a function of the parameter of interest only and not of the nuisance parameters. The estimator for π is found by maximizing the profile likelihood

$$\hat{\pi} = \operatorname{argmax}_{\pi} L_\pi(\hat{\theta}_\pi) = \operatorname{argmax}_{\pi} L(\pi, \hat{\theta}_\pi). \quad (\text{B.12})$$

Consider now the profile likelihood ratio $\lambda(\pi)$ constructed from the profile likelihood and the maximum likelihood:

$$\lambda(\pi) = \frac{L(\pi, \hat{\theta}_\pi)}{L(\hat{\pi}, \hat{\theta})}, \quad (\text{B.13})$$

where it should be noted that $\hat{\theta}$ represents the global best estimate of each nuisance parameter. A convenient test statistic for a hypothesized value of π is:

$$t_\pi = -\log \lambda(\pi). \quad (\text{B.14})$$

From Eq. (B.13), the profile ratio λ must fall in the range $0 \leq \lambda \leq 1$, with values near 1 implying good agreement between the data and the hypothesized value of π . In turn,

higher values of t_π indicate that the hypothesized value of π is inconsistent with the data.

The log-likelihood is frequently employed as a test statistic in counting experiments. Because the distributions that make up the likelihood in Eq. (B.18) are exponential, what were products in the likelihood become sums in the log-likelihood, simplifying calculations substantially.

Another simplification to estimating the parameter of interest is by use of the Asimov data set. This representative data set is used to evaluate the Asimov likelihood L_A and corresponding profile likelihood ratio λ_A :

$$\lambda_A(\pi) = \frac{L_A(\pi, \hat{\boldsymbol{\theta}}_\pi)}{L_A(\hat{\pi}, \hat{\boldsymbol{\theta}})} = \frac{L_A(\pi, \hat{\boldsymbol{\theta}}_\pi)}{L_A(\pi', \boldsymbol{\theta})}, \quad (\text{B.15})$$

where π' is the mean value of π given by the Monte Carlo simulation, and $\boldsymbol{\theta}$ are the known (or assumed) values of the nuisance parameters.

There is uncertainty associated with parameter estimation. The central confidence interval $[a, b] = [\hat{\pi} - c, \hat{\pi} + d]$ is the interval in which the true value of π has equal probability of being in the interval $[c, \pi]$ or $[\pi, d]$. As discussed in [82], even if the likelihood function is not a Gaussian function of the parameters, as in this case where L is composed of the product of Poisson and Gaussian distributions, the central confidence interval can still be approximated using

$$-\log L(\hat{\pi}_{-c}^{+d}) = -\log L_{max} + \frac{N^2}{2}, \quad (\text{B.16})$$

where $N = \Phi^{-1}(1 - \alpha/2)$ is the quantile of the standard Gaussian corresponding to the desired confidence level $1 - \alpha$.

The number of events n observed in counting experiments in particle physics follow a Poisson probability distribution with mean and variance ν as shown in Eq. (B.8). In the analysis described in this dissertation, the signature of interest is composed of both signal and background events with expected means s and b , and thus $\nu = s + b$. The systematic uncertainties of signal and background events are treated as following a Gaussian probability density function with mean μ and variance σ^2 :

$$P(m|\mu, \sigma^2) = \frac{1}{\sqrt{2\pi}\sigma} \exp\left[-\frac{1}{2}\left(\frac{m - \mu}{\sigma}\right)^2\right]. \quad (\text{B.17})$$

For the signal and background uncertainties, it is assumed that $m - \mu = 1$, and the variance is $\sigma_s^2 = 0.1, 0.2$, or 0.3 for the signal. Similarly, for the background uncertainty, the variance is taken to be $\sigma_b^2 = 0.1$.

The likelihood function, $L(n|s, b, \sigma_s^2, \sigma_b^2)$, defines the probability of observing the number of events n given the parameters s, b, σ_s^2 , and σ_b^2 :

$$L(n|s, b, \sigma_s^2, \sigma_b^2) = \left(\frac{(s+b)^n}{n!} e^{-(s+b)}\right) \left(\frac{1}{\sqrt{2\pi}\sigma_s} e^{-\frac{1}{2}\left(\frac{1}{\sigma_s}\right)^2}\right) \left(\frac{1}{\sqrt{2\pi}\sigma_b} e^{-\frac{1}{2}\left(\frac{1}{\sigma_b}\right)^2}\right) \quad (\text{B.18})$$

Of the four parameters, I am only interested in finding \hat{s} , the best estimate of s , and $\sigma_{\hat{s}}$, the variance of this estimate of s , based on the number of events n observed. The parameters, b, σ_s^2 , and σ_b^2 , are nuisance parameters.

I run two trials of Monte Carlo simulations to obtain two sets of estimates for s and b . The representative Asimov data set is built from the estimates of s and b from Trial 1 as well as from the assumed systematic uncertainties $\sigma_s = 0.1$ and $\sigma_b = 0.1$. Trial 2 plays the role of the experiment, and its estimates comprise the ‘‘observed’’ number of events $n = s + b$. With values for n, s, b, σ_s , and σ_b for the likelihood in Eq. (B.18),

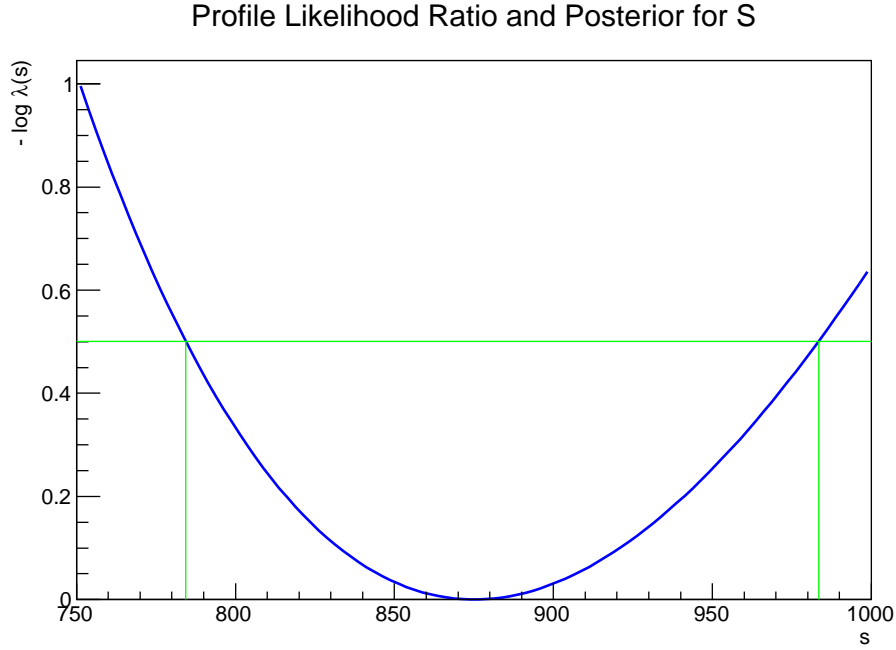


Figure B.1: The blue curve is the distribution of the profile likelihood ratio for $R^{-1} = 800$ GeV, $\Lambda R = 20$, with $g_{ued} = g_{sm}$. Minimizing the profile likelihood ratio identifies the expected number of signal events. The green horizontal line identifies movement of $1/2$ away from the minimum. The values of s corresponding to this movement away from the minimum given the upper and lower limits of the confidence interval with 68.3% coverage.

I utilized the profile ratio calculator implemented in the `RooStats` package of `ROOT` to numerically minimize $-\log \lambda(s)$, where $\lambda(s)$ is the profile likelihood ratio constructed from the Asimov data set. To find the central confidence interval of s with 68.3% coverage, I plot the profile likelihood ratio vs. s and find the values of s that satisfy Eq. (B.16) with $N = \Phi^{-1}(1 - \alpha/2) = 1$ as is seen in Figure B.1. I repeat this procedure for 95.4% coverage, where the bounds on this confidence interval are the values of s that correspond to moving away from the minimum of $-\log \lambda$ by 2 units. I can then again find these confidence intervals when $\sigma_s = 0.2$ or 0.3 . The entire procedure is done for

each variation of g_{ued} at each point in the parameter space of $800 \text{ GeV} \leq R^{-1} \leq 1300 \text{ GeV}$, $\Lambda R = 20$, and at $R^{-1} = 800 \text{ GeV}$, $\Lambda R = 5$.

B.2 Estimating cut efficiencies and their uncertainties using Bayesian statistics

Searching for a signature of interest involves selecting events that pass selection criteria (i.e., cuts) designed to maximize the contribution from signal processes to the signature while minimizing contributions from background processes. The selection efficiency, ϵ , is the conditional probability that an event will pass the cut. Because the true efficiency of the cut is not known, the efficiency must be estimated. This estimate for the efficiency is made from repeated trials of applying the cut, in which k events are selected out of n independent trials. Because each event either succeeds or fails in passing the cut, k is binomially distributed with a probability of success, ϵ :

$$P(k|n, \epsilon) = \frac{n!}{k!(n-k)!} \epsilon^k (1-\epsilon)^{n-k}. \quad (\text{B.19})$$

To find $P(\epsilon|k, n)$, the probability that the true value of the efficiency is in the interval $(\epsilon, \epsilon + d\epsilon)$, apply Bayes' theorem:

$$P(\epsilon|k, n) = \frac{P(k|n, \epsilon)P(\epsilon|n)}{Z}. \quad (\text{B.20})$$

Here, $P(\epsilon|n)$ is the probability that ϵ is the “true” value of the efficiency before the data, k , are taken, and Z is a normalization constant. A reasonable choice for the prior, $P(\epsilon|n)$, is a uniform distribution on the interval $[0, 1]$ [84]. This follows from the fact

that event selection follows a binomial process, forcing the efficiency to fall somewhere in the stated range, while at the same time, there is no reason to prefer any particular value within that range. Given a uniform prior, Z can be calculated (as shown in [84]), and the result is:

$$P(\epsilon|k, n) = \frac{\Gamma(n+2)}{\Gamma(k+1)\Gamma(n-k+1)} \epsilon^k (1-\epsilon)^{n-k}. \quad (\text{B.21})$$

The peak of this distribution is k/n , and this is the estimate for the efficiency.

Because $P(\epsilon|k, n)$ is not generally symmetric, particularly for values of k close to 0, as is the case in this analysis, using the square root of the variance to measure the uncertainty of the estimate of the efficiency will not ensure that the probability of finding the true value of ϵ within the interval will be 68.3% as it would with a normal distribution. Instead, a measurement of the asymmetric errors can be made by finding the smallest credible interval $[a, b] \subset [0, 1]$ with posterior probability λ , such that the minimization of the interval $b - a$ is constrained by:

$$\int_a^b P(\epsilon|k, n) d\epsilon = \lambda \quad (\text{B.22})$$

If such an interval can be found for $\lambda = 68.3\%$, then the uncertainty can be understood in much the same way as a quote of $\pm 1\sigma$ as for a normal distribution.

The solution for a and b can be found formally using the method of Lagrange

multipliers [84, 85]. This is done by simultaneously solving the non-linear equations:

$$\begin{aligned}
C + \rho a^k (1 - a)^{n-k} &= 0 \\
C + \rho b^k (1 - b)^{n-k} &= 0 \\
B_a(k + 1, n - k - 1) - B_b(k + 1, n - k - 1) &= C\lambda,
\end{aligned}
\tag{B.23}$$

where $C = \Gamma(k + 1)\Gamma(n - k + 1)/\Gamma(n + 2)$, ρ is the Lagrange multiplier, and λ is the desired probability content of the confidence interval. The last line features the incomplete Beta function, $B_x(u, v)$, defined by:

$$B_x(u, v) = \int_0^x t^{u-1} (1 - t)^{v-1} dt.
\tag{B.24}$$

Finding the solution is non-trivial. Fortunately, a solution has been implemented in `ROOT` under the `TEfficiency::Bayesian()` class.

To test the consistency of results from the Monte Carlo generators and my signal selection algorithms, I tested the compatibility of trials 1 and 2 in each variation of g_{ued}/g_{sm} for each R^{-1} and ΛR . I did this by assessing the asymmetric uncertainties of the cut efficiencies for each trial, then comparing trial 1 to trial 2 to ensure that the trials were in agreement with each other within 68.3% to 95.4%. Additionally, I conducted two trials of each SM background, $t\bar{t}$ and $W^\pm W^\pm jj$ and made a similar comparison of the trials.

Looking for good agreement between the two trials for each g_{ued}/g_{sm} , I checked the consistency of the efficiency of each cut described in Section (cutflow table) as well as the efficiency of all cuts applied compared to the initial number of events generated.

Cut applied	ϵ_1	ϵ_2	Z score
mUED signal events generated	0.0904 ± 0.0006	0.0906 ± 0.0006	0.266
trigger	0.204 ± 0.003	0.207 ± 0.003	1.054
like-sign leptons	0.227 ± 0.007	0.232 ± 0.007	0.758
2 hard jets	0.245 ± 0.015	$0.249^{+0.015}_{-0.014}$	0.288
missing p_T	$0.663^{+0.032}_{-0.033}$	$0.677^{+0.031}_{-0.032}$	0.433
all cuts/mUED signal events generated	$0.0075^{+0.0007}_{-0.0006}$	0.0081 ± 0.0007	0.937

Table B.1: Cut efficiencies for signal events for mUED scenario: $R^{-1} = 800$ GeV, $\Lambda R = 20$ ($g_{ued}/g_{sm} = 1$) for trials 1 and 2 which served as the model and observed events respectively.

The results in Table B.1 show that in most cases the uncertainties are symmetric around the estimate for the efficiency k/n , and when the uncertainties are asymmetric, they are barely so. Treating the uncertainties from Trial 1 as symmetric and labeling them as σ_1 , the Z -score is defined as:

$$Z = \frac{\epsilon_1 - \epsilon_2}{\sigma_1}. \quad (\text{B.25})$$

The Z -scores in Table B.1 are typical of the results across all trials of varying g_{ued} . The Z -score varied between 0.015 and 5.545, being above 3.0 only six times (out of 210 Z -scores calculated) and was below 2.0 80% of the time.

Bibliography

- [1] **ATLAS** Collaboration, G. Aad *et al.*, “Observation of a new particle in the search for the Standard Model Higgs boson with the ATLAS detector at the LHC,” *Phys.Lett.* **B716** (2012) 1–29, [arXiv:1207.7214 \[hep-ex\]](#).

- [2] **CMS** Collaboration, S. Chatrchyan *et al.*, “Observation of a new boson at a mass of 125 GeV with the CMS experiment at the LHC,”
Phys.Lett. **B716** (2012) 30–61, [arXiv:1207.7235 \[hep-ex\]](#).

- [3] **Planck** Collaboration, P. Ade *et al.*, “Planck 2013 results. XVI. Cosmological parameters,” *Astron.Astrophys.* **571** (2014) A16,
[arXiv:1303.5076 \[astro-ph.CO\]](#).

- [4] P. Fayet, “Supersymmetry and Weak, Electromagnetic and Strong Interactions,”
Phys.Lett. **B64** (1976) 159.

- [5] P. Fayet, “Spontaneously Broken Supersymmetric Theories of Weak, Electromagnetic and Strong Interactions,” *Phys.Lett.* **B69** (1977) 489.

- [6] G. R. Farrar and P. Fayet, “Phenomenology of the Production, Decay, and

- Detection of New Hadronic States Associated with Supersymmetry,”
Phys.Lett. **B76** (1978) 575–579.
- [7] N. Arkani-Hamed, S. Dimopoulos, and G. Dvali, “The Hierarchy problem and new dimensions at a millimeter,” *Phys.Lett.* **B429** (1998) 263–272, [arXiv:hep-ph/9803315](#) [hep-ph].
- [8] I. Antoniadis, N. Arkani-Hamed, S. Dimopoulos, and G. Dvali, “New dimensions at a millimeter to a Fermi and superstrings at a TeV,”
Phys.Lett. **B436** (1998) 257–263, [arXiv:hep-ph/9804398](#) [hep-ph].
- [9] I. Antoniadis, “A Possible new dimension at a few TeV,”
Phys.Lett. **B246** (1990) 377–384.
- [10] D. B. Kaplan and H. Georgi, “SU(2) x U(1) Breaking by Vacuum Misalignment,”
Phys.Lett. **B136** (1984) 183.
- [11] D. B. Kaplan, H. Georgi, and S. Dimopoulos, “Composite Higgs Scalars,”
Phys.Lett. **B136** (1984) 187.
- [12] L. Randall and R. Sundrum, “A Large mass hierarchy from a small extra dimension,” *Phys.Rev.Lett.* **83** (1999) 3370–3373, [arXiv:hep-ph/9905221](#) [hep-ph].
- [13] T. Appelquist, H.-C. Cheng, and B. A. Dobrescu, “Bounds on universal extra dimensions,” *Phys.Rev.* **D64** (2001) 035002, [arXiv:hep-ph/0012100](#) [hep-ph].

- [14] H.-C. Cheng, K. T. Matchev, and M. Schmaltz, “Bosonic supersymmetry? Getting fooled at the CERN LHC,” *Phys.Rev.* **D66** (2002) 056006, [arXiv:hep-ph/0205314](#) [hep-ph].
- [15] S. Glashow, “Partial Symmetries of Weak Interactions,” *Nucl.Phys.* **22** (1961) 579–588.
- [16] S. Weinberg, “A Model of Leptons,” *Phys.Rev.Lett.* **19** (1967) 1264–1266.
- [17] A. Salam, “Weak and Electromagnetic Interactions,” in *Elementary particle theory: Relativistic groups and analyticity*, Svartholm, Nils, ed., pp. 367–377. Almqvist & Wiksell.
- [18] B. W. Lee and S. Weinberg, “Cosmological Lower Bound on Heavy Neutrino Masses,” *Phys.Rev.Lett.* **39** (1977) 165–168.
- [19] G. Steigman, “Cosmology Confronts Particle Physics,” *Ann.Rev.Nucl.Part.Sci.* **29** (1979) 313–338.
- [20] N. Arkani-Hamed, A. G. Cohen, and H. Georgi, “Electroweak symmetry breaking from dimensional deconstruction,” *Phys.Lett.* **B513** (2001) 232–240, [arXiv:hep-ph/0105239](#) [hep-ph].
- [21] N. Arkani-Hamed, A. G. Cohen, and H. Georgi, “(De)constructing dimensions,” *Phys.Rev.Lett.* **86** (2001) 4757–4761, [arXiv:hep-th/0104005](#) [hep-th].
- [22] H.-C. Cheng and I. Low, “TeV symmetry and the little hierarchy problem,” *JHEP* **0309** (2003) 051, [arXiv:hep-ph/0308199](#) [hep-ph].

- [23] H.-C. Cheng and I. Low, “Little hierarchy, little Higgses, and a little symmetry,” *JHEP* **0408** (2004) 061, [arXiv:hep-ph/0405243](#) [hep-ph].
- [24] G. Servant and T. M. Tait, “Is the lightest Kaluza-Klein particle a viable dark matter candidate?,” *Nucl.Phys.* **B650** (2003) 391–419, [arXiv:hep-ph/0206071](#) [hep-ph].
- [25] H.-C. Cheng, J. L. Feng, and K. T. Matchev, “Kaluza-Klein dark matter,” *Phys.Rev.Lett.* **89** (2002) 211301, [arXiv:hep-ph/0207125](#) [hep-ph].
- [26] B. A. Dobrescu and E. Poppitz, “Number of fermion generations derived from anomaly cancellation,” *Phys.Rev.Lett.* **87** (2001) 031801, [arXiv:hep-ph/0102010](#) [hep-ph].
- [27] T. Appelquist, B. A. Dobrescu, E. Ponton, and H.-U. Yee, “Proton stability in six-dimensions,” *Phys.Rev.Lett.* **87** (2001) 181802, [arXiv:hep-ph/0107056](#) [hep-ph].
- [28] T. Kaluza, “On the Problem of Unity in Physics,” *Sitzungsber.Preuss.Akad.Wiss.Berlin (Math.Phys.)* **1921** (1921) 966–972.
- [29] O. Klein, “Quantum Theory and Five-Dimensional Theory of Relativity. (In German and English),” *Z.Phys.* **37** (1926) 895–906.
- [30] O. Klein, “The Atomicity of Electricity as a Quantum Theory Law,” *Nature* **118** (1926) 516.

- [31] T. Appelquist, B. A. Dobrescu, E. Ponton, and H.-U. Yee, “Neutrinos vis-a-vis the six-dimensional standard model,” *Phys.Rev.* **D65** (2002) 105019, [arXiv:hep-ph/0201131](#) [[hep-ph](#)].
- [32] **Super-Kamiokande** Collaboration, H. Nishino *et al.*, “Search for Proton Decay via $p \rightarrow e^+ \pi_0$ and $p \rightarrow \mu^+ \pi_0$ in a Large Water Cherenkov Detector,” *Phys.Rev.Lett.* **102** (2009) 141801, [arXiv:0903.0676](#) [[hep-ex](#)].
- [33] T. G. Rizzo, “Pedagogical introduction to extra dimensions,” *eConf* **C040802** (2004) L013, [arXiv:hep-ph/0409309](#) [[hep-ph](#)].
- [34] D. Hooper and S. Profumo, “Dark matter and collider phenomenology of universal extra dimensions,” *Phys.Rept.* **453** (2007) 29–115, [arXiv:hep-ph/0701197](#) [[hep-ph](#)].
- [35] H.-C. Cheng, K. T. Matchev, and M. Schmaltz, “Radiative corrections to Kaluza-Klein masses,” *Phys.Rev.* **D66** (2002) 036005, [arXiv:hep-ph/0204342](#) [[hep-ph](#)].
- [36] J. M. Cornell, S. Profumo, and W. Shepherd, “Dark matter in minimal universal extra dimensions with a stable vacuum and the right Higgs boson,” *Phys.Rev.* **D89** no. 5, (2014) 056005, [arXiv:1401.7050](#) [[hep-ph](#)].
- [37] **ATLAS** Collaboration, “Search for squarks and gluinos in events with isolated leptons, jets and missing transverse momentum at $\sqrt{s} = 8$ TeV with the ATLAS detector,” ATLAS-CONF-2013-062, ATLAS-COM-CONF-2013-039.

- [38] M. Blennow, H. Melbeus, T. Ohlsson, and H. Zhang, “RG running in a minimal UED model in light of recent LHC Higgs mass bounds,” *Phys.Lett.* **B712** (2012) 419–424, [arXiv:1112.5339 \[hep-ph\]](#).
- [39] T. Kakuda, K. Nishiwaki, K.-y. Oda, and R. Watanabe, “Universal extra dimensions after Higgs discovery,” *Phys.Rev.* **D88** (2013) 035007, [arXiv:1305.1686 \[hep-ph\]](#).
- [40] V. Branchina, E. Messina, and M. Sher, “Lifetime of the electroweak vacuum and sensitivity to Planck scale physics,” *Phys.Rev.* **D91** (2015) 013003, [arXiv:1408.5302 \[hep-ph\]](#).
- [41] **ATLAS** Collaboration, “Search for squarks and gluinos with the ATLAS detector in final states with jets and missing transverse momentum and 20.3 fb^{-1} of $\sqrt{s} = 8 \text{ TeV}$ proton-proton collision data,” ATLAS-CONF-2013-047, ATLAS-COM-CONF-2013-049.
- [42] C. Macesanu, “The Phenomenology of universal extra dimensions at hadron colliders,” *Int.J.Mod.Phys.* **A21** (2006) 2259–2296, [arXiv:hep-ph/0510418 \[hep-ph\]](#).
- [43] K. R. Dienes, E. Dudas, and T. Gherghetta, “Grand unification at intermediate mass scales through extra dimensions,” *Nucl.Phys.* **B537** (1999) 47–108, [arXiv:hep-ph/9806292 \[hep-ph\]](#).
- [44] J. Papavassiliou and A. Santamaria, “Chiral fermions and gauge fixing in

- five-dimensional theories,” *Phys.Rev.* **D63** (2001) 125014,
arXiv:hep-ph/0102019 [hep-ph].
- [45] A. Pukhov, “CalcHEP 2.3: MSSM, structure functions, event generation, batchs,
and generation of matrix elements for other packages,”
arXiv:hep-ph/0412191 [hep-ph].
- [46] A. Datta, K. Kong, and K. T. Matchev, “Minimal Universal Extra Dimensions in
CalcHEP/CompHEP,” *New J.Phys.* **12** (2010) 075017,
arXiv:1002.4624 [hep-ph].
- [47] B. C. Allanach, S. Grab, and H. E. Haber, “Supersymmetric Monojets at the
Large Hadron Collider,” *JHEP* **1101** (2011) 138, arXiv:1010.4261 [hep-ph].
- [48] **LHC Higgs Cross Section Working Group** Collaboration, A. David *et al.*,
“LHC HXSWG interim recommendations to explore the coupling structure of a
Higgs-like particle,” arXiv:1209.0040 [hep-ph].
- [49] A. Freitas, P. Z. Skands, M. Spira, and P. Zerwas, “Examining the identity of
Yukawa with gauge couplings in supersymmetric QCD at LHC,”
JHEP **0707** (2007) 025, arXiv:hep-ph/0703160 [HEP-PH].
- [50] A. Freitas and P. Z. Skands, “Testing the SUSY-QCD Yukawa coupling in a
combined LHC/ILC analysis,” *Pramana* **69** (2007) 843–848,
arXiv:hep-ph/0609180 [hep-ph].
- [51] A. Belyaev, M. Brown, J. Moreno, and C. Papineau, “Discovering Minimal

- Universal Extra Dimensions (MUED) at the LHC,” *JHEP* **1306** (2013) 080, [arXiv:1212.4858](#).
- [52] M. Bahr, S. Gieseke, M. Gigg, D. Grellscheid, K. Hamilton, *et al.*, “Herwig++ Physics and Manual,” *Eur.Phys.J.* **C58** (2008) 639–707, [arXiv:0803.0883 \[hep-ph\]](#).
- [53] H.-L. Lai, M. Guzzi, J. Huston, Z. Li, P. M. Nadolsky, *et al.*, “New parton distributions for collider physics,” *Phys.Rev.* **D82** (2010) 074024, [arXiv:1007.2241 \[hep-ph\]](#).
- [54] J. Butterworth, G. Dissertori, S. Dittmaier, D. de Florian, N. Glover, *et al.*, “Les Houches 2013: Physics at TeV Colliders: Standard Model Working Group Report,” [arXiv:1405.1067 \[hep-ph\]](#).
- [55] M. Dobbs and J. B. Hansen, “The HepMC C++ Monte Carlo event record for High Energy Physics,” *Comput.Phys.Commun.* **134** (2001) 41–46.
- [56] R. Brun and F. Rademakers, “ROOT: An object oriented data analysis framework,” *Nucl.Instrum.Meth.* **A389** (1997) 81–86.
- [57] M. Cacciari, G. P. Salam, and G. Soyez, “FastJet User Manual,” *Eur.Phys.J.* **C72** (2012) 1896, [arXiv:1111.6097 \[hep-ph\]](#).
- [58] M. Cacciari and G. P. Salam, “Dispelling the N^3 myth for the k_t jet-finder,” *Phys.Lett.* **B641** (2006) 57–61, [arXiv:hep-ph/0512210 \[hep-ph\]](#).

- [59] M. Cacciari, G. P. Salam, and G. Soyez, “The Anti-k(t) jet clustering algorithm,” *JHEP* **0804** (2008) 063, [arXiv:0802.1189 \[hep-ph\]](#).
- [60] S. Frixione, P. Nason, and G. Ridolfi, “A Positive-weight next-to-leading-order Monte Carlo for heavy flavour hadroproduction,” *JHEP* **0709** (2007) 126, [arXiv:0707.3088 \[hep-ph\]](#).
- [61] P. Nason, “A New method for combining NLO QCD with shower Monte Carlo algorithms,” *JHEP* **0411** (2004) 040, [arXiv:hep-ph/0409146 \[hep-ph\]](#).
- [62] S. Frixione, P. Nason, and C. Oleari, “Matching NLO QCD computations with Parton Shower simulations: the POWHEG method,” *JHEP* **0711** (2007) 070, [arXiv:0709.2092 \[hep-ph\]](#).
- [63] S. Alioli, P. Nason, C. Oleari, and E. Re, “A general framework for implementing NLO calculations in shower Monte Carlo programs: the POWHEG BOX,” *JHEP* **1006** (2010) 043, [arXiv:1002.2581 \[hep-ph\]](#).
- [64] J. Alwall, M. Herquet, F. Maltoni, O. Mattelaer, and T. Stelzer, “MadGraph 5 : Going Beyond,” *JHEP* **1106** (2011) 128, [arXiv:1106.0522 \[hep-ph\]](#).
- [65] **ATLAS** Collaboration, “Calibration of the performance of b -tagging for c and light-flavour jets in the 2012 ATLAS data,” ATLAS-CONF-2014-046, ATLAS-COM-CONF-2013-087.
- [66] **CMS** Collaboration, S. Chatrchyan *et al.*, “Search for new physics in events with

- same-sign dileptons and jets in pp collisions at $\sqrt{s} = 8$ TeV,”
JHEP **1401** (2014) 163, [arXiv:1311.6736](#).
- [67] **ATLAS** Collaboration, “Review of the ATLAS Technical design report on the forward detectors for the measurement of elastic scattering and luminosity,”
 CERN-LHCC-2008-013, LHCC-G-140.
- [68] **ATLAS** Collaboration, I. Efthymiopoulos, “Elastic cross-section and luminosity measurement in ATLAS at LHC,” [arXiv:hep-ex/0510078](#) [[hep-ex](#)].
- [69] J. Pumplin, D. Stump, R. Brock, D. Casey, J. Huston, *et al.*, “Uncertainties of predictions from parton distribution functions. 2. The Hessian method,”
Phys.Rev. **D65** (2001) 014013, [arXiv:hep-ph/0101032](#) [[hep-ph](#)].
- [70] J. Pumplin, D. Stump, J. Huston, H. Lai, P. M. Nadolsky, *et al.*, “New generation of parton distributions with uncertainties from global QCD analysis,”
JHEP **0207** (2002) 012, [arXiv:hep-ph/0201195](#) [[hep-ph](#)].
- [71] H.-L. Lai, J. Huston, Z. Li, P. Nadolsky, J. Pumplin, *et al.*, “Uncertainty induced by QCD coupling in the CTEQ global analysis of parton distributions,”
Phys.Rev. **D82** (2010) 054021, [arXiv:1004.4624](#) [[hep-ph](#)].
- [72] **LHC/LC Study Group** Collaboration, G. Weiglein *et al.*, “Physics interplay of the LHC and the ILC,” *Phys.Rept.* **426** (2006) 47–358,
[arXiv:hep-ph/0410364](#) [[hep-ph](#)].

- [73] **CMS** Collaboration, G. Sieber, “ α_s extraction and PDF constraints from jet measurements at CMS,” *PoS DIS2014* (2014) 030.
- [74] G. Cowan, K. Cranmer, E. Gross, and O. Vitells, “Asymptotic formulae for likelihood-based tests of new physics,” *Eur.Phys.J.* **C71** (2011) 1554, [arXiv:1007.1727 \[physics.data-an\]](#).
- [75] L. Moneta, K. Belasco, K. S. Cranmer, S. Kreiss, A. Lazzaro, *et al.*, “The RooStats Project,” *PoS ACAT2010* (2010) 057, [arXiv:1009.1003 \[physics.data-an\]](#).
- [76] M. Aliev, H. Lacker, U. Langenfeld, S. Moch, P. Uwer, *et al.*, “HATHOR: HAdronic Top and Heavy quarks crOss section calculatoR,” *Comput.Phys.Commun.* **182** (2011) 1034–1046, [arXiv:1007.1327 \[hep-ph\]](#).
- [77] S. Moch and P. Uwer, “Theoretical status and prospects for top-quark pair production at hadron colliders,” *Phys.Rev.* **D78** (2008) 034003, [arXiv:0804.1476 \[hep-ph\]](#).
- [78] A. Martin, W. Stirling, R. Thorne, and G. Watt, “Parton distributions for the LHC,” *Eur.Phys.J.* **C63** (2009) 189–285, [arXiv:0901.0002 \[hep-ph\]](#).
- [79] T. Flacke, K. Kong, and S. C. Park, “A Review on non-minimal universal extra dimensions,” *Mod.Phys.Lett.* **A30** no. 05, (2015) 1530003, [arXiv:1408.4024 \[hep-ph\]](#).

- [80] A. De Rujula, A. Donini, M. Gavela, and S. Rigolin, “Fat brane phenomena,” *Phys.Lett.* **B482** (2000) 195–204, [arXiv:hep-ph/0001335](#) [hep-ph].
- [81] **ATLAS** Collaboration, G. Aad *et al.*, “Search for diphoton events with large missing transverse momentum in 7 TeV proton-proton collision data with the ATLAS detector,” *Phys.Lett.* **B718** (2012) 411–430, [arXiv:1209.0753](#) [hep-ex].
- [82] G. Cowen, *Statistical Data Analysis*. Oxford University Press, New York, 1998.
- [83] M. H. DeGroot, *Probability and Statistics*. Addison-Wesley, United States, 2nd ed., 1986.
- [84] M. Paterno, “Calculating efficiencies and their uncertainties,” FERMILAB-TM-2286-CD.
- [85] D. Casadei, “Estimating the selection efficiency,” *JINST* **7** (2012) P08021, [arXiv:0908.0130](#) [physics.data-an].